ORIGINAL PAPER

Recent progress in experiments on the heaviest nuclides at SHIP

Michael Block[1,2,3] · **Francesca Giacoppo**[1,2] · **Fritz-Peter Heßberger**[1,2] · **Sebastian Raeder**[1,2]

© The Author(s) 2022

Abstract

Understanding the atomic and nuclear properties of very heavy and superheavy nuclides is one of the main objectives in experiments at the recoil separator SHIP at the GSI Helmholtzzentrum für Schwerionenforschung in Darmstadt, Germany. This article summarizes recent experiments performed on isotopes of the elements with $Z = 102$–105. The radionuclides of interest were produced in heavy-ion fusion-evaporation reactions with lead and bismuth targets and separated from the primary beam by the velocity filter SHIP. The studies by α–γ spectroscopy experiments, direct mass measurements and laser spectroscopy employed the SHIP decay-spectroscopy setup, the new COMPASS detector, the mass spectrometer SHIPTRAP, and the laser spectroscopy setup RADRIS. This article briefly introduces the experimental approaches and discusses selected results providing a more comprehensive picture of the nuclear structure around the deformed neutron shell closure at $N = 152$. Future perspectives to extend such experiments towards other regions in the heaviest nuclei will also be addressed.

1 Introduction

The GSI Helmholtzzentrum für Schwerionenforschung in Darmstadt, Germany, is a center for accelerator-based fundamental research which was established more than

✉ Michael Block
m.block@gsi.de

1   GSI Helmholtzzentrum für Schwerionenforschung, Planckstr. 1, 64291 Darmstadt, Germany

2   Helmholtz Institute Mainz, Staudingerweg 18, 55118 Mainz, Germany

3   University of Mainz, Fritz-Strassmann-Weg 2, 55128 Mainz, Germany

50 years ago. One of the driving scientific motivations at that time was the search for superheavy elements (SHE). The existence of these nuclei with $Z > 103$ was predicted in the late 1960s [1, 2] based on theoretical models extending the nuclear shell model [3, 4]. These models explained the stability of superheavy nuclei (SHN) by nuclear shell effects that provide an increased binding energy by as much as 10 MeV to stabilize them against spontaneous fission. One of the most striking features in the early predictions was the existence of a region of superheavy nuclei near spherical proton and neutron shell closures at $Z = 114$ and $N = 184$ [1, 2] where the half-lives would exceed 10^9 years (with a partial fission half-life of 10^{16} years) [5]. This region was coined *island of stability*.

Reaching this island motivated significant experimental efforts in the following decades that resulted in the discovery of new elements up to oganesson with $Z = 118$ [6–8]. Evidence confirming the existence of the island of stability was indeed obtained from increasing half-lives of more neutron-rich superheavy isotopes [8]. However, more recent theoretical predictions suggest that the longest half-lives on this island will only be on the order of 100 years [9]. This is still remarkable for very exotic nuclides, but it rules out that SHE exist in nature. Nonetheless, SHE remain a forefront topic of nuclear physics research and many scientific questions remain open. Some of these questions and the theoretical description of SHE are discussed in several review articles, see for example the recent work by Giuliani et al. [10] and references therein.

Present experimental efforts do, however, not only concentrate on the production of new elements. Instead, the nuclear structure evolution in SHN is studied in detail, which is indispensable for answering fundamental questions about the nature of the strong interaction itself. Accurate experimental data on various nuclear properties such as, e.g., decay characteristics, energies of excited states, nuclear moments, the strength and location of shell effects, and many others provide insight into the underlying physics and challenge theoretical predictions, eventually leading to an improvement of the models.

Theoretical predictions of the heaviest nuclei were initially predominantly made by nuclear models using macroscopic-microscopic approaches in which the macroscopic description is based on the nuclear drop model [11] and shell-correction energies are introduced by an approach proposed by Strutinsky [12]. All models of this type predict the location of spherical proton and neutron shell closures to occur at $Z = 114$ and $N = 184$, see e.g. Ref. [13].

Self-consistent models using energy-density functionals, e.g., Skyrme-Hartree-Fock-Bogoliubov (SHFB) models and relativistic mean-field models (RMF) [14, 15], have been applied to SHE since the late 1990s. Most of these models predict a spherical proton shell closure at $Z = 120$, but other functionals also obtain it at $Z = 114$ (SkI4), or even at $Z = 126$ (SkP, SkM*). There is generally a better agreement among the models with respect to the location of the spherical neutron shell closure that most of them predict to occur at $N = 184$, except for a number of RMF models that obtain a shell closure at $N = 172$.

Several authors have discussed how the location of these shell closures depends on details in the description of the underlying nuclear forces, for example on the values of the effective mass m^* and the strength of the spin-orbit interaction. This has been discussed, for instance, by Rutz et al. [14] and by Bender et al. [16]. It has also been

emphasized [16] that for self-consistent models using energy-density functionals the energy gap between the spin-orbit partners $2f_{5/2}$ and $2f_{7/2}$ may result in a shift of the maximum proton shell gap from $Z = 114$ to $Z = 120$.

The experimental strategy to benchmark these different theoretical models and to constrain some of their parameters is to obtain many different nuclear structure observables of nuclei in this region to provide information on the shell structure and the deformation. This is for example accomplished by systematic studies of nuclear masses, changes in mean square charge radii, and the measurement of the energies of excited nuclear states.

The low production rates of SHN and the resulting low number of events remain a major challenge in all experimental investigations. Still today, the only viable production scheme for superheavy elements are complete fusion-evaporation reactions. The resulting cross sections for evaporation residues are on the order of tens of nanobarn for the production of Rf isotopes and drop steeply to a level of one picobarn for Og. Even for high primary-beam intensities of $> 6 \times 10^{12}$ particles per second as they are routinely delivered by the Universal Linear Accelerator (UNILAC) of GSI the corresponding yield for experiments is only in the range of few particles per minute or even some particles per week.

Therefore, a prerequisite for all experiments investigating these rare nuclei is an electromagnetic recoil separator providing a high suppression of primary beam-related particles while at the same time featuring a high transmission for evaporation residues. Consequently, the velocity filter SHIP [17] was one of the first experimental installations at the GSI to enable a superheavy-element-research program. The kinematic separation with SHIP is briefly described in Sect. 2.1. The design of SHIP and the experiments performed in the first 25 years of its operation that also led to the discovery of six superheavy elements with $Z = 107$–112 have been discussed in several previous reviews, see for example the review by Hofmann and Münzenberg [6, 18], and are not subject of this article.

The experimental capabilities for a comprehensive SHE research program addressing the atomic and nuclear structure of the heaviest nuclides in the region $Z = 100$–110 around the deformed neutron shell closures at $N = 152$ and $N = 162$ were expanded in recent years. Nuclides investigated in recent experiments at SHIP as discussed in this article are depicted in Fig. 1. High-precision mass spectrometry and laser spectroscopy were introduced to the region of the heaviest elements at SHIP. These two complementary techniques offer new possibilities to observe the nuclear structure evolution, for example by studying shell closures via masses, by identifying long-lived isomers by mass spectrometry, and to determine nuclear spins and electromagnetic moments with laser spectroscopy. As already mentioned earlier, with these studies we can obtain a more complete picture of the structure of the heaviest nuclides.

To carry out this research program, we operate a suite of versatile instrumentation comprising the COMPASS detection system for $\alpha - \gamma$ spectroscopy in the focal plane of SHIP [19, 20], the Penning-trap mass spectrometer SHIPTRAP for direct high-precision mass measurements [21], and the RAdiation Detected Resonant Ionization Spectroscopy (RADRIS) setup [22, 23] for laser spectroscopy. Here, we review selected recent experiments on neutron-deficient isotopes of the elements No-Db carried out with the above-mentioned techniques in recent years. Section 2.2 gives a brief
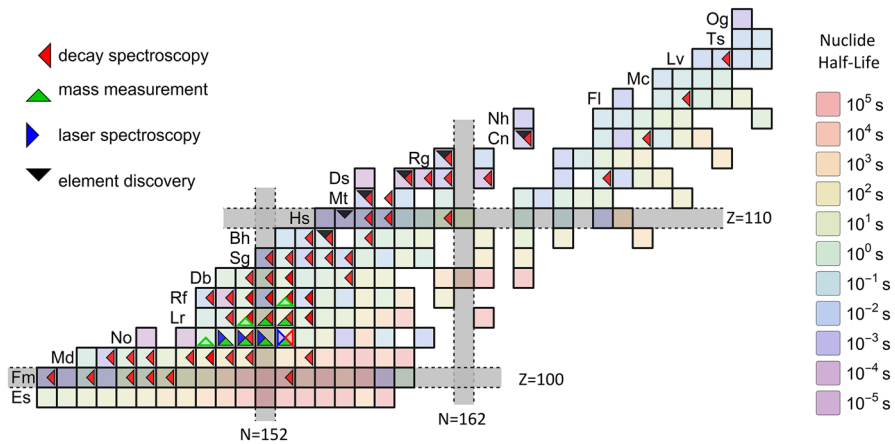
Fig. 1 Excerpt of the nuclear chart showing the region of the heaviest elements color-coded by the half-life of the nuclides. Besides the isotopes from the early element discovery campaigns at SHIP, the nuclides studied at SHIP in experiments with decay spectroscopy, mass measurements and laser spectroscopy, respectively, are indicated by the colored triangles. Open symbols indicated nuclides where the data analysis is ongoing and a publication is in preparation

introduction to the nuclide production utilizing fusion-evaporation reactions. Mass measurements with SHIPTRAP and a discussion on some results are presented in Sect. 2.3. Section 2.4 presents the basics principles of laser spectroscopy together with the results of the first laser spectroscopy campaign in transfermium elements. In Sect. 2.5 the determination of nuclear properties from $\alpha-\gamma$ spectroscopy data is discussed, while Sect. 3 provides a brief summary and some conclusions.

## 2 Experimental approaches and employed setups

2.1 The velocity filter SHIP

The two-stage velocity filter SHIP [17] (Separator for Heavy Ion reaction Products) has been the workhorse in Superheavy Element (SHE) research at GSI for about 45 years. The setup is schematically shown in Fig. 2.

It was designed for the investigation of products from complete-fusion reactions, so-called evaporation residues (ER), induced by heavy projectiles ($A > 40$). Main design goals of the construction were to obtain a high transmission for the evaporation residues and an effective suppression of the projectile beam. The basic principle of the separation method is to use the velocity difference between projectiles and ER, which is given by

$$v_{ER} \approx v_{CN} = (m_p/(m_p + m_t)) \times v_p = (m_p/m_{CN}) \times v_p . \qquad (1)$$

Here v_{CN}, v_{ER}, v_p denote the velocities of the compound nucleus (CN), the ER and the projectile (p), respectively. m_p, m_t, m_{CN} are the masses of the projectile, the target
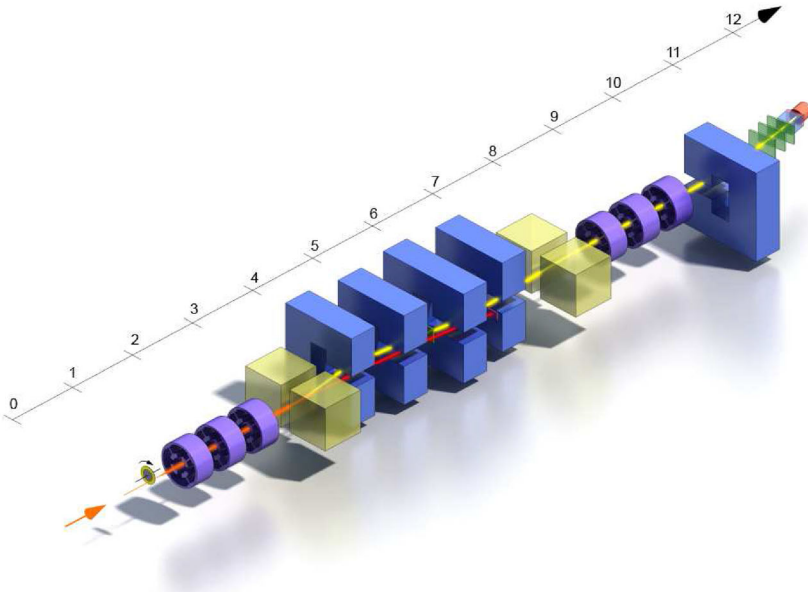
Fig. 2 The present setup of the velocity-filter SHIP at GSI Darmstadt. Separation of recoils (yellow trajectories) from the primary beam (red trajectories) is achieved by their velocity through an arrangement of crossed electric fields, produced with two pairs of condenser plates (yellow blocks), and magnetic fields created by dipole magnets (blue). Two magnetic quadrupole tripletts (purple) shape the ion beam and a final dipole magnet (blue) improves the separation from scattered particles before the recoils reach the Time-of-Flight detectors (green) and the detector array. The scale on the left indicates the length in meters. Reprinted with permission from Block [21]

(t) nucleus and the compound nucleus. Evidently the ER velocity is always lower than the projectile velocity.

The force F acting on an ion of charge q moving in a combination of crossed homogeneous magnetic (B) and electric (E) fields, arranged to deflect in opposite directions, is described by

$$F = q \times (v \times B - E). \tag{2}$$

This effective force vanishes for ions with a velocity of $v = (E/B)$ so that they will be transmitted through the combination of electromagnetic fields, while ions of any other velocity are deflected.

Due to the reaction kinematics the distribution of the ER is peaked in forward direction and therefore SHIP was aligned in direction of the primary beam. It was believed at the time of construction that SHE would be preferentially produced in rather symmetric reactions, where ER are sharply focused in forward direction. Therefore, a small entrance aperture of $\pm 1.5°$ in axial and radial direction was chosen to effectively suppress products from transfer reactions, which have a larger angular distribution. The technical layout was characterized by the following requirements:

(a) Complete separation of the projectile beam from the ER
(b) Collecting nearly all charge states of the ER

(c) Accepting at best the complete range of the ER velocity distributions
(d) High transmission
(e) Stigmatic focussing
(f) Velocity dispersion at the exit
(g) Technical feasibility, specifically the operation of high-voltage condensers up to 600 kV (≈ 4.0 MV/m) that was technically challenging at the time of the construction.

Taking all these requirements into account the separator was designed as a two stage velocity filter with separated electric and magnetic fields in the arrangement: quadrupole triplet–HV condenser–four dipole magnets–HV condenser–quadrupole triplet. SHIP accepts a relative velocity width of $\pm 5\%$ and a charge-state width of $\pm 10\%$. The HV condenser was chosen as the first dispersive element for technical reasons. As projectiles always have larger radii of curvature they are less deflected. So, even in case of a HV breakdown the projectiles will not hit the condenser plates, which could lead to severe damages when high beam intensities of, e.g., 1 pµA (6×10^{12} particles per second) are used. The dipole magnets are of C-type with parallel entrance and exit field boundaries. So it is possible to vary all deflection angles and also the dispersion from zero to the maximum value. For experiments needing deflection voltages exceeding the maximum attainable, this is an important option.[1] The separated ions appear to pass undeflected through the field arrangement as long as the deflection angles are small. As the deflection fields of the magnets are only weakly focussing each stage was complemented with a quadrupole triplet.

The first filter stage is followed by a velocity slit, where an intermediate focus is produced by the first quadrupole triplet and the ER are already spatially separated from the projectile beam. The components of the second stage of the filter are arranged symmetrically to those of the first one with the plane of the velocity slit as the mirror plane and are operated anti-symmetrically, so that the velocity dispersions in both stages are added together [24].

After it turned out that rather symmetric reactions, e.g., ^{136}Xe + ^{170}Er → ^{306}122*, are not the successful way to produce SHE [25] the strategy of 'cold fusion' reactions [26] using targets around doubly magic ^{208}Pb and medium-heavy projectiles (^{54}Cr,^{58}Fe) to synthesize the new elements with $Z = (107–109)$ was followed. So-called cold-fusion reactions comprise combinations of heavy-ions beams with Pb and Bi targets resulting in a low excitation energy of the compound nucleus on the order of 10–20 MeV. For this excitation energy range, besides prompt fission of the compound nucleus, the de-excitation by one to two neutrons has the highest probability. It turned out that for these less symmetric reactions with a larger angular distribution of the ER, the small entrance aperture was a bottle neck, limiting the SHIP transmission to $\leq 30\%$. To proceed to heavier elements thus an increase of the transmission was necessary. The latter could be achieved by moving the target position as close as possible to the entrance of the first quadrupole. An increase by a factor of roughly two could be expected [27]. The prize to pay, however, was increased background of scattered projectiles passing SHIP with the ER-velocity. A sufficient suppression could be achieved by adding a dipole magnet of weak dispersion behind the second

---

[1] at standard operation deflection of the ER in the HV condenser is 0.1 rad

quadrupole triplet [28]. A deflection of 7.5^0 resulted to be a good compromise to remove unwanted particles and to avoid a significant transmission loss for ER. This configuration was since then adopted as standard operation mode.

The separation time is given by the flight-time through SHIP, which strongly depends on the mass ratio between projectile and target nuclei; for ^{254}No from the reaction ^{208}Pb(^{48}Ca,2n)^{254}No one obtains a value of $T_{\text{flight}} \approx 2.3$ µs, while for ^{270}Ds from the reaction ^{207}Pb(^{64}Ni,n)^{270}Ds a significantly lower value of $T_{\text{flight}} \approx 1.4$ µs is obtained.

In cold-fusion reactions for synthesis of SHE usually lead or bismuth are used as target material. The melting points of 600.61 K for lead and 544.4 K for bismuth render some difficulties in their use when high beam currents on the order of 10^{12}–10^{13} particles are required. Due to the deposited heat from the primary beam, fixed targets made of 'simple' foils will be destroyed immediately. Therefore, a target wheel rotating synchronously to the beam-pulse structure (5 ms, 50 Hz repetition rate) has been developed [29]. Target quality, size and performance have been continuously improved. In the present version [30] eight target segments are mounted on a wheel of 356 mm outer diameter and an 'effective' diameter of 310 mm with respect to the beam-spot position, rotating at a speed of 1125 rpm. The individual target segments that are mounted on such a wheel have a length of 120 mm and a height of 26 mm.[2] The material is evaporated or sputtered on a carbon layer of typically 40 µg/cm^2 and covered with a carbon layer of typically 10 µg/cm^2 to improve radiative cooling and to prevent sputtering of target material during irradiation; typical thicknesses of the lead or bismuth layers are $\approx$500 µg/cm^2. The use of metallic lead or bismuth limited the beam intensity, so the use of compounds was considered. In particular, PbS (1397 K melting point) and Bi$_2$O$_3$ (1100 K melting point) were identified as good choices [31]. To obtain homogeneous layers, the carbon-layer foil is heated during the production process to about 570 K. PbS targets turned out to be very robust and were irradiated with ^{40}Ar ions up to 3 pµA (1.86×10^{13}/s); Bi$_2$O$_3$ targets are less stable, they could be irradiated with ^{40}Ar ions up to 1.5 pµA.

The target quality is controlled on-line [32], using a 20 keV electron beam and measuring the attenuation of the current after passing the targets. Changes of structure can be resolved at a resolution of < 0.5 mm at a target velocity of 20 m/s. Sweeping the electron beam in radial direction enables to detect pinholes, changes of the effective thickness etc. over the whole target area.

2.2 Production of the nuclides of interest by fusion-evaporation reactions and separation from the primary beam by SHIP

The method of complete-fusion reactions, i.e. the total amalgamation of projectile and target nuclei has been so far the only successful way to produce isotopes of heaviest elements. For such complete-fusion reactions the energy relation depends on the kinetic energy of the projectile E_p and is given by

$$E^* = E_{\text{CM}} + Q \tag{3}$$

---

[2] 'open' length and height, without frames
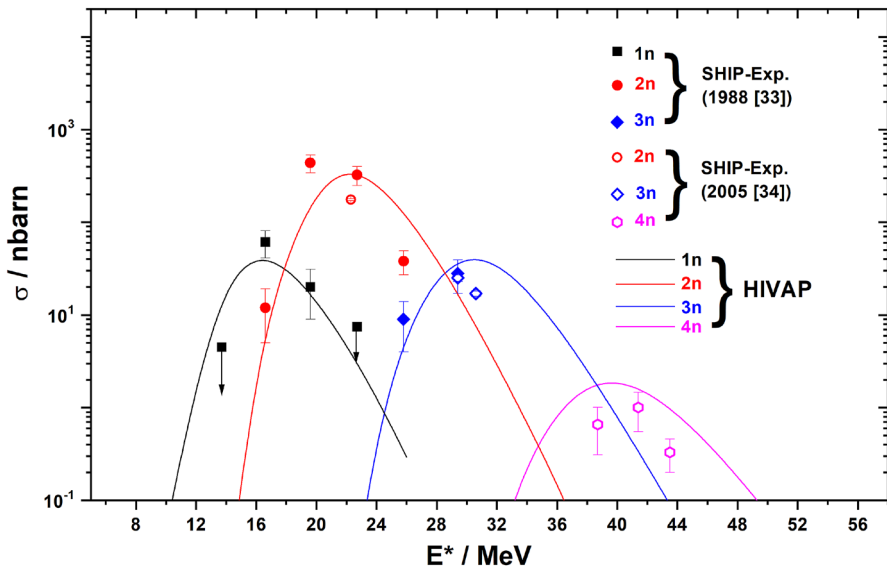
Fig. 3 Excitation function for the reaction ^{48}Ca + ^{209}Bi showing the most populated evaporation channels. Reprinted by Heßberger [34]. The symbols represent experimental data taken from [33, 34] while the lines are results from calculations using the HIVAP code. The HIVAP code has been described in Ref. [35].

Here, E_{CM} is the kinetic energy in the center-of-system, $Q = (m_p + m_t - m_{CN})c^2$ is the Q value of the reaction and E^* the excitation energy of the CN.

As both, projectile and target nuclei carry a positive electric charge, a minimum energy has to be applied to overcome the Coulomb barrier and bring both into contact. It is usually defined as the value where the probability for complete fusion is 0.5, which refers to a half density overlap of both reaction partners and is denoted as fusion barrier. For the production of superheavy nuclei using medium-heavy projectiles such as ^{50}Ti, ^{54}Cr, ^{58}Fe etc. and heavy target nuclei such as ^{208}Pb, ^{238}U, ^{248}Cm, etc., this simple description is not valid anymore.

At energies around the fusion barrier there is a strong competition between complete amalgamation of target and projectile nuclei resulting in a fully equilibrated mono-nucleus (compound nucleus) and binary processes leading to a strong exchange of nucleons or at best to a very short-lived mono-nucleus that reseparates already before mass and charge equilibrium has been reached. This is referred to as quasi fission. This reduction of the fusion probability is often denoted as fusion hindrance. In addition, superheavy nuclei are purely shell stabilized as liquid-drop fission barriers have vanished. Shell effects, however, are washed out at increasing excitation energies, and thus the survival probability of the compound nuclei drops rapidly at increasing excitation energies.

As a consequence there is only a narrow energy window favorable for the production of isotopes of the heaviest elements. For detailed investigations it is thus crucial to have information on the optimum energy at which the production cross sections are maximal. This is obtained measuring the production rates as function of the bombard-

ing energy (or excitation energy) over a wide range. The result for such a measurement is shown in Fig. 3 for the so-called cold-fusion reaction ^{209}Bi(^{48}Ca,xn)$^{257-x}$Lr. Data are taken from [33, 34].

Evidently, the maximum cross-section is obtained for the 2n-channel (^{255}Lr) while it is dropping by about an order of magnitude for the 1n-channel (^{256}Lr) due to a decrease of the fusion probability towards lower energies, and the 3n-channel (^{254}Lr) due to increasing fission probability of the CN, a further steep decrease by a factor of about 40 is found for the 4n-channel. The lines are the results of calculations using the HIVAP code [35]. Parameters (sub-barrier fusion probability, fission barrier) were here adopted to reproduce the 1n- and 2n-cross sections. Evidently the trend of decreasing cross sections for increasing excitation energies is reproduced reasonably well.

It should be noted, however, that ^{48}Ca + ^{209}Bi is still a 'favorable' case. For heavier systems (in cold-fusion reactions), despite of lower fusion probabilities, 1n-channels dominate and energy regions for optimum production become even smaller.

Somewhat different conditions are found for 'hot' fusion reactions, used for the synthesis of elements $Z = 114$–118, using ^{48}Ca-projectiles and actinide targets in the range $Z = 94$–98, where due to lower 'fusion hindrance' maxima of the cross sections are found at higher excitation energies ($E^* \approx 30$–40 MeV) and excitation functions are broader. For details we refer to [8].

2.3 Mass spectrometry with SHIPTRAP

Penning-trap mass spectrometry (PTMS) is a well-established technique for nuclear structure studies. It relies on the direct connection and the absolute nuclear binding energy that can be obtained via accurate measurements of the atomic mass. Thus, systematic trends of masses, for example along isotopic chains, reveal signatures of nuclear shell structure and the onset of deformation [36]. High-precision mass measurements also provide a powerful method to identify (long-lived) isomeric states and pin down their excitation energy accurately as shown in several cases [37–41]. PTMS is suited for investigating long-lived isomers with half-lives of at least fifty milliseconds, a limit given by the time required for ion preparation. Due to the relation of the achievable mass resolving power with the available measurement time there is a tradeoff between highest resolution and shortest half-life to be made. However, for half-lives on the order of half a second and beyond the identification of states with low excitation energies is straightforward. This is of great interest in heavy nuclei that predominantly decay by internal conversion and for the identification of α-decaying isomers with similar half-lives of the isomeric state and the ground state. Besides revealing the nuclear structure evolution, direct mass measurements in the heaviest elements provide anchor points to fix the decay chains in the mass surface. Mass spectrometry techniques can also support the identification of (new) nuclides based on their mass-to-charge ratio, provided a sufficiently high mass resolving power can be achieved. This is specifically valuable if the decay modes or the half-life of the nuclide prevents the observation of correlated decay events. Combining the results from direct mass measurements with Q values from decay spectroscopy enables us to improve the mass values of heavier members of a decay chain. These may be inaccessible
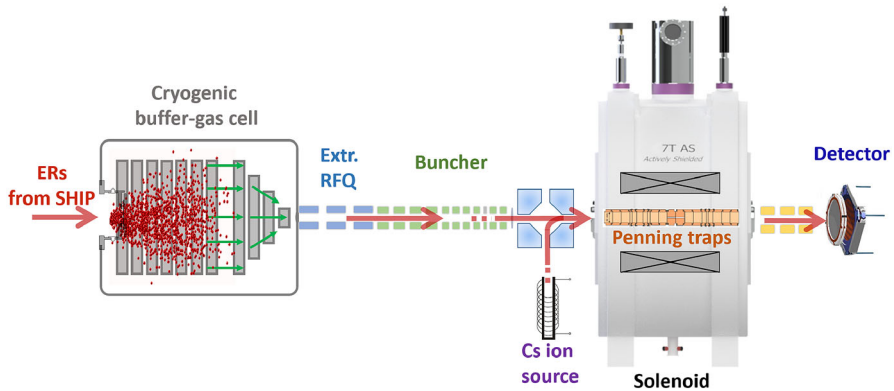
Fig. 4 Schematic layout of the SHIPTRAP setup. The ion beam enters a cryogenic stopping cell. From there, ions are extracted into a radiofrequency quadrupole section for stacking, cooling and bunching. The ion bunches are injected into a double Penning trap system inside a 7-T solenoid

to direct mass spectrometry either due to half-life limitations or due to low yields. However, this requires that the decay schemes are well known. This is usually the case in even-even nuclides where the strongest α decay occurs from the ground state of the mother nucleus to the ground state in the daughter. In odd-odd and odd-A nuclei the strongest α-decay branch connects states with the same configuration, which is typically an excited state in the daughter. Here, a mass measurement can provide an independent result for the Q value.

PTMS is well described in the literature, see for example the reviews on PTMS of radionuclides by Blaum [42] and the review by Kluge [43]. A more general discussion on precision measurements of radionuclides has been presented by Blaum et al. [44]. The status of PTMS in the region of the heaviest elements has been recently discussed by Block [21, 45]. Thus, here only a very brief introduction will be given with emphasis on aspects that are peculiar for mass measurements of the heaviest elements.

The installation of SHIPTRAP, a Penning trap behind SHIP, was proposed more than 20 years ago to probe the structure of heavy and superheavy nuclei via direct mass measurements [46]. This proposal was based on emerging techniques that paved the way for the efficient preparation of radionuclides from fusion-evaporation reactions as brilliant low-energy bunched beams facilitating an efficient injection into a Penning trap. One of the prerequisites was the buffer-gas-stopping technique to slow down particle beams with tens of MeV kinetic energy in an inert buffer-gas environment at pressures of around 50 mbar in less than one meter length [47–49]. The second ingredient was the application of radio-frequency quadrupole (RFQ) structures serving as cooler-buncher devices. This approach had been pioneered at ISOLTRAP [50]. It enables the cooling, stacking, and bunching of ions in helium buffer gas at moderate density (typical pressures are on the order of 10^{-3} mbar). In this way, radioactive ions can be accumulated and prepared in parallel to an ongoing measurement in a Penning trap.

The schematic layout of SHIPTRAP is presented in Fig. 4. The first part is the second-generation buffer-gas stopping cell that is operated at about 45 K [49] for

maximum cleanliness. The reaction products enter this cell after separation from the primary beam by SHIP through a thin-foil entrance window. This is made out of a low-Z material, typically titanium, and its thickness is chosen for each experiment according to the stopping range of the fusion products of interest. The typical thickness for Ti foils is on the order of 3 μm. Additional degrader foils may be inserted in front of the window to adapt the range. The window diameter of about 60 mm is adapted to the size of the spatial distribution of the reaction products at this position. The ions are then stopped in ultra-pure helium gas at about 50–70 mbar (room-temperature equivalent). The stopped ions remain in a charge state of 1+, 2+, or 3+ depending on their ionization potential [51]. They are extracted with electric fields that ensure the fast and efficient transport of the ions towards the exit. A funnel structure with a superimposed RF field prevents the ions from hitting the walls and focuses them onto a de-Laval nozzle of 0.6 mm diameter from which they are extracted in a supersonic jet of the buffer gas. A detailed description of the gas cell is given elsewhere [48, 49].

The extracted ions enter an RFQ structure operated as ion guide transporting them to an RFQ cooler buncher. This consists of four axially segmented rods to form a potential gradient along the RFQ with a potential well at the end. The ions are cooled within few milliseconds in collisions with helium buffer-gas atoms and are accumulated in the potential well for a variable time adapted to the measurement cycle in the Penning traps. Ions can be stacked in the RFQ over times up to seconds. The ions are extracted as short bunches with low energy spread. The bunch length and the energy spread can be adapted to the requirements of an efficient capturing scheme in the Penning trap by varying the operation conditions of the cooler buncher.

A set of electrostatic ion-optical elements comprising einzel lenses and deflectors forms the transport section providing the ion bunches to the Penning-trap system. Two cylindrical traps are installed in the room-temperature bore of a superconducting 7 T-solenoid that features two homogenous regions. This double-trap concept was established at SHIPTRAP and is also employed at TRIGA-TRAP [52] and JYFLTRAP [53], for example. The installation of two Penning traps in one solenoid is cost efficient and simplifies the ion transport between the two traps. The first trap, the so-called purification trap, is used to remove unwanted reaction products and cool the ions of interest employing the well-established buffer-gas-cooling technique [54]. Depending on the experimental conditions such as the excitation amplitudes and the cycle time, mass resolving powers of $m/\Delta m \approx 100,000$ are achieved. This is usually sufficient to separate nuclear isobars. The separation of isobars is important to assure a pure ion sample for the following precision measurement. The presence of nuclear isobars is less of an issue for the heaviest nuclei produced by rather selective fusion-evaporation reactions where the production of isobars is usually suppressed due to the narrow excitation functions. Isobars may be 'produced' in electron-capture decays of the ion of interest during the storage in the trap. This can be detected in the measurement trap due to the high resolving power. An exception are isobars that may be produced during the storage and preparation of ions in the RFQ buncher and the purification trap by electron-capture decay for nuclides with half-lives on the order of the typical cycle times. The preparation of pure and well-cooled samples is also one of the prerequisites for high-precision measurement of the cyclotron frequency. For example, the cooling

of the ions of interest in the first trap assures a minimal axial energy spread and a close-to-zero magnetron radius.

The measurement trap is connected to the purification trap by an orifice with 1 mm diameter and 51 mm length that acts as pumping barrier. A mass measurement is performed based on the determination of the trapped ion's cyclotron frequency ν_c with the phase-imaging ion-cyclotron-resonance (PI-ICR) technique. This powerful method was introduced at SHIPTRAP a few years ago [55, 56]. The cyclotron frequency of a trapped ion is obtained from a measurement of the phase of its radial motion. To this end, an excitation to a certain radius is performed applying an external RF field in a suitable geometry, followed by a free evolution for a defined (trapping) time until the extraction from the trap. To measure the phase, the radial ion motion is imaged on a position-sensitive ion detector. At SHIPTRAP, a commercial micro-channel plate detector with delay-line anode is used. A detailed explanation of the method and relevant systematic uncertainties has been given previously [55, 56]. The PI-ICR approach has meanwhile become the new standard in PTMS of radionuclides due to its supreme performance with extremely high mass resolving power, a lower number of ions required to obtain a mass value compared to the former standard, the time-of-flight ion-cyclotron-resonance (ToF-ICR) method [57] and no need for an excitation-frequency scan. Low statistical mass uncertainties of a few 10^{-9} are achieved for radionuclides as demonstrated in several experiments, in particular for mass difference measurements and for measurements of mass doublets [39, 40, 58]. Compared to ToF-ICR as used in the first mass measurements on nobelium and lawrencium isotopes at SHIPTRAP, PI-ICR provides a forty times higher mass resolving power for the same measurement time [55]. This is of particular importance for measurements of heavy nuclides and allows the identification of low-lying nuclear isomers. Note that a relative mass uncertainty of 5 keV for mass $A = 250$ corresponds to a relative precision of $\delta m/m = 2 \times 10^{-8}$. A gain in precision in PTMS can also be achieved by using higher charge states. However, charge breeding in an electron-beam ion trap, as for example used at TITAN [59], is (presently) not an option for the low ion rates handled with SHIPTRAP. However, due to the high cleanliness of cryogenic gas-stopping cells one can often profit from doubly and, in some cases, triply charged ions for mass measurements.

One limitation in PTMS is given by the need of calibrating the magnetic field strength B at the position of the ion of interest with high accuracy. This is usually accomplished by a measurement of the cyclotron frequency ν_{c-ref} of a reference ion with well-known mass before and after the measurement of the ion of interest. In addition, this reference ion should have a mass-to-charge ratio similar to the ion of interest to avoid systematic uncertainties related to inhomogeneities of the trapping fields [60]. However, this may become challenging in the region of the heaviest elements due to the limited number of heavy reference ions with well-known mass. This is mitigated as most of the ions can be measured in a 2+ charge state so that $^{133}Cs^+$ is a suitable calibrant ion with a mass-to-charge ratio sufficiently close to limit mass-dependent systematic uncertainties.

Another challenge is related to the magnetic-field stability that may become an issue for measurements on nuclides with low yield as for the heaviest nuclides that results in measurement times of several hours or even a few days. This is only feasible

if additional measures are taken to improve the temporal stability of the electric and magnetic trapping fields. An indirect stabilization of the magnetic field is achieved by regulating the magnet-bore temperature and the pressure of the magnet's cryostat as employed at SHIPTRAP for several years [61]. The system has been recently improved further to reach a typical stability of the bore temperature of better than 10 mK and a pressure stability of the magnet's (LHe) cryostat within 0.1 mbar. This minimizes the impact on the cyclotron-frequency measurements to a level that is below the typical statistical uncertainty.

Continuous efforts to boost the performance of SHIPTRAP led to an overall efficiency on the level of 5–10% [49]. This value is mainly limited by the detection efficiency of the position-sensitive detector of about 30% and the charge-state distribution of ions extracted from the cryogenic gas cell. For ions with a high ionization potential, additional losses may occur by charge exchange with residual impurities in the RFQ buncher and the Penning trap. Mass measurements with lowest ion rates are furthermore limited by background that may arise from detector dark counts and by ions created in the radioactive decay of the ions of interest. Under typical experimental conditions at SHIPTRAP individual measurements can be performed with detected ion rates on the order of one ion per day. If a lower precision suffices, for example if only a mass number determination was required, then even lower rates could be handled.

2.3.1 SHIPTRAP results

The on-line commissioning of the initial SHIPTRAP setup with the first-generation gas stopping cell [47] was carried out in 2004 with isotopes of rare earth elements [62]. The following measurement campaigns focused on nuclides along the pathway of the astrophysical rapid proton-capture process that are favorably produced in fusion-evaporation reactions [63, 64]. In this way, for example, the mass of the nuclide ^{85}Mo, with $N = Z + 1$ was measured directly. Later on, the region of proton emitters among the rare-earth elements with mass numbers $A \approx 150$ was investigated. Direct mass measurements provided accurate values of the proton-separation energy and allowed us to determine the location of the proton drip line in Tm and Ho. It should be noted that not all proton-unbound nuclides with $S_p < 0$ show proton emission in their ground states as the partial half-live of the β decay branch is often shorter than that of the proton decay [65]. The nuclide with the lowest cross section that had been measured in that campaign was the proton emitter ^{147}Tm with a cross section of about 100–200 μbarn.

The first SHIPTRAP measurement campaign in the region of the heaviest elements was performed in 2008 when the mass of several nobelium isotopes starting from ^{254}No were measured directly for the first time [66]. These measurements were extended up to ^{256}Lr [67]. The results obtained until 2012 have been discussed in previous reviews [21, 45] and are only briefly summarized here. In recent years, the measurements have been further extended towards heavier and ever-more rare nuclides in on-line measurement campaigns within the FAIR phase-0 program following a relocation of the SHIPTRAP setup [68]. A major performance improvement results from the integration of the cryogenic stopping cell. The new arrangement allowed us to inject the
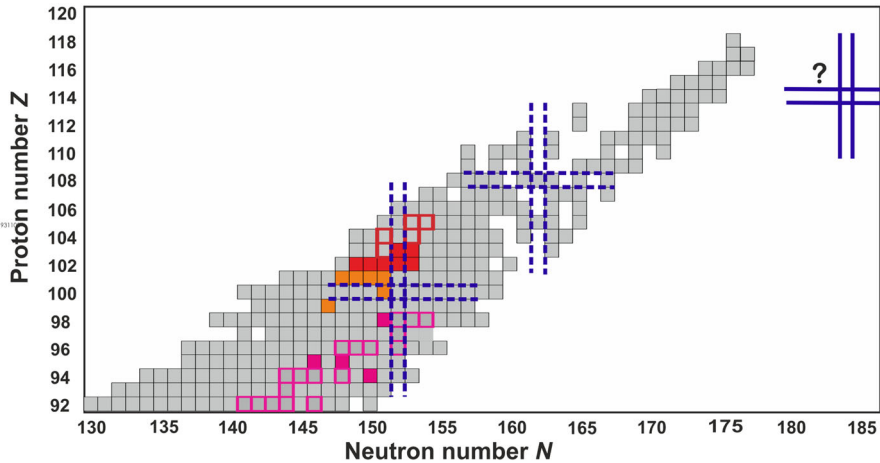
Fig. 5 Direct mass measurements in the region of the heaviest nuclides. Direct measurements with TRIGA-TRAP [69] (magenta), SHIPTRAP [66, 67] (red) and the RIKEN MR-ToF [70] (orange) are marked in color. Measurements that are planned or have been performed but are yet unpublished are indicated by the open squares (Reprinted figure (with permission adapted from Block [45], Fig. 1))

heavy ions of interest along the symmetry axis of the gas cell, whereas in the previous configuration the secondary ion beam had to be injected perpendicular to the extraction axis limiting the overall efficiency of the SHIPTRAP setup. The higher efficiency of the gas cell and its improved cleanliness together with the PI-ICR technique increased the sensitivity for mass measurements with SHIPTRAP significantly. Improved mass values for previously studied nobelium and lawrencium isotopes will become available soon as well as first direct mass measurements of ^{251}No, ^{254}Lr, ^{257}Rf, and ^{258}Db. In several cases also low-lying isomeric states have been resolved. The data analysis of the recent campaigns is still ongoing and first publications of the new data are in preparation. The measurements demonstrated that masses of nuclides produced with cross sections on the level of few nanobarn can be measured with SHIPTRAP. The heavy nuclides in the transuranium region that have been measured with SHIPTRAP are shown in Fig. 5.

The SHIPTRAP results are complemented by mass measurements of lighter actinides with the TRIGA-TRAP Penning trap in Mainz [52]. These actinide isotopes are still available in weighable quantities facilitating off-line measurements with a laser-ablation ion source. In addition to the previously published TRIGA-TRAP results on Pu and Am isotopes [69], additional actinides are being investigated in an ongoing measurement campaign. These are displayed by the open magenta squares in Fig. 5. TRIGA-TRAP can presently measure nuclides for which samples containing at least 10^{15} atoms for the laser-ablation ion source are available.

Mass spectrometry of heavy radionuclides are nowadays also performed by the the KEK group working at RIKEN/GARIS using a so-called multi-reflection time-of-flight mass spectrometers [70, 71]. These devices reach mass resolving powers up to about 600,000 by extending the flight path in the spectrometer by reflecting ion bunches multiple times between electrostatic mirrors. The flight times of ions in such devices
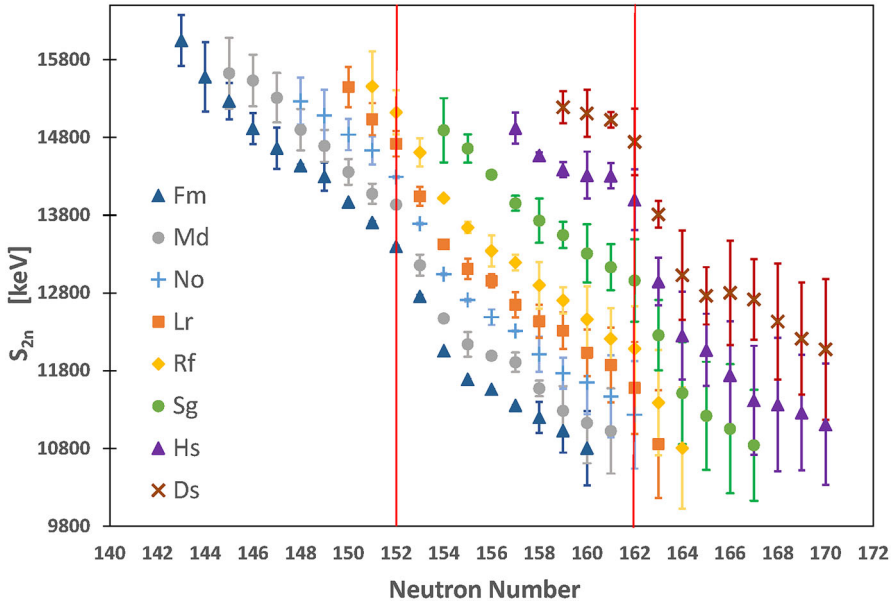
Fig. 6 Two-neutron separation energies of selected heavy elements between Fm and Ds around the deformed neutron shell closures at $N = 152$ and $N = 162$ indicated by the red vertical lines

are on the order of ten milliseconds and precision of about $\delta m/m \approx 5 \times 10^{-8}$–$10^{-7}$ have been reached [71–74]. The fast measurement scheme gives access to short-lived nuclei but the reduced mass resolving power compared to PTMS is insufficient to resolve isomeric states with low excitation energies that often exist in the heaviest nuclei. In recent years the KEK group has performed mass measurements of Fm and Md isotope behind the GARIS separator at RIKEN [70] and recently reported a first measurement in ^{257}Db with limited statistics [75].

Taking the latest data from direct mass measurements and other indirect techniques as they were considered in the atomic mass evaluation (AME 2020) [76] the nuclear-structure evolution around the deformed neutron shell closure at $N = 152$ can be studied. The visibility of this nuclear closure is enhanced by using so-called mass filters, i.e., a specific binding-energy difference. A commonly used one is the two-neutron separation energy S_{2n}. The two-nucleon-separation energies are favorable to display the gross nuclear-structure evolution compared to the one-nucleon-separation energies that feature the odd-even staggering reflecting the pairing interaction. A plot of the two-neutron separation energies of selected elements from Fm to Ds for neutron numbers from $N = 140$–170 is shown in Fig. 6. The presented data include the earlier SHIPTRAP results of direct mass measurements of nobelium and lawrencium isotopes [66, 67, 77] but not the yet unpublished results of the latest campaigns.

The S_{2n} values decrease smoothly with increasing N as expected and show a steeper drop at neutron numbers $N = 152$ and $N = 162$ where deformed shell closures are known to occur [78]. The size of the kink at the shell closure is indicative of the size of the shell gap and can be better visualized by the so-called empirical (neutron/proton)

Table 1 Production schemes and fusion-evaporation cross sections for isotopes of interest for SHIPTRAP measurements

Nuclide	Half-life (s)	Reaction	Cross section (nb)
^{255}Rf	1.68(9)	^{50}Ti(^{207}Pb, 2n)	11.4 [80]
^{257g}Db	2.3(2)	^{50}Ti(^{209}Bi, 2n)	2.3 [81]
^{257m}Db	0.67(6)	^{50}Ti(^{209}Bi, 2n)	2.3 [81]
^{258g}Db	1.9(5)	^{50}Ti(^{209}Bi, 1n)	4.4 [82]
^{258m}Db	4.3(5)	^{50}Ti(^{209}Bi, 1n)	4.4 [82]
^{259}Sg	0.28(5)	^{54}Cr(^{207}Pb, 2n)	0.42 [82]
^{261}Sg	0.18	^{54}Cr(^{208}Pb, 1n)	2.5 [83]
^{262}Bh	0.083	^{54}Cr(^{209}Bi, 1n)	0.29 [82]
^{269}Hs	9.7	^{26}Mg(^{248}Cm, 5n)	0.007 [84]
^{270}Hs	22	^{26}Mg(^{248}Cm, 4n)	0.003 [84]

The lifetimes are taken from the Evaluated Nuclear Structure Data Files [79]. The given cross-sections are either taken from literature where references are given or evaluated based on previous SHIP experiments

shell gap $\delta_{2n/2p}$. However, also in Fig. 6 it is seen that the strength of the shell gap at $N = 152$ changes in different elements and is largest in Fm at $Z = 100$. It should be noted that the strength of the deformed shell closures at $N = 152, 162$ is much smaller than the typical value obtained for a strong spherical shell closure such as the one at $N = 126$, for example, where the corresponding values is about 8 MeV. The general observation is that in the heaviest nuclides there are no longer distinct magic numbers but rather regions of extended shell stabilization. This has been also studied with several theoretical models, see for example the discussion by Bender et al. [16].

2.3.2 SHIPTRAP outlook

In this section, perspectives for future mass measurements with SHIPTRAP are addressed. Based on the present efficiency level of a few percent, measurements on nuclides produced with cross sections on the nanobarn level are feasible with SHIP-TRAP. Future upgrades along with the availability of a new accelerator that will provide ten times higher primary-beam intensity are expected to push this limit to a level of 10–100 pb. This opens up a number of new perspectives for direct mass measurements on nuclides with higher Z. A selection of suitable nuclear reactions for producing such isotopes is summarized in Table 1.

The majority of the given reactions utilizes lead and bismuth targets and has already been used at SHIP in decay spectroscopy experiments. These reactions lead to the production of neutron-deficient isotopes that are often too short-lived to be accessible with SHIPTRAP. This concerns for example the region beyond Sg around the deformed shell closure at $N = 162$ that is mostly out of reach with SHIPTRAP, except for the long-lived Hs isotopes ^{269,270}Hs [84], which already require the use of Cm targets. Also, the production of other more neutron-rich isotopes that are typically longer-lived requires hot-fusion reactions with radioactive actinide targets. In the case of Hs, an

option would be for example ^{26}Mg(^{248}Cm,xn)^{269,270}Hs with a cross section of only 3 picobarn for ^{270}Hs. However, there are some technical challenges that have to be overcome. In the past the only actinide targets that have been used in experiment at SHIP comprise ^{238}U and ^{248}Cm that were irradiated with beams of ^{48}Ca, ^{54}Cr, and ^{64}Ni in experiments on copernicium, livermorium and in the search for element $Z = 120$ a few years ago [85, 86]. Due to the larger angular distribution and the design of SHIP as discussed in Sect. 2.1, the transmission through SHIP decreases with increasing asymmetry of the nuclear reaction and drops rather steep for a ratio of projectile-to-target mass below 0.1. For ^{48}Ca-induced reactions with ^{238}U and ^{248}Cm the SHIP transmission is still on the order of 15–30% but drops for more asymmetric reactions such as ^{22}Ne on ^{197}Au to only about 5%. A second challenge for SHIPTRAP experiments is the low recoil energy that does not allow the use of pinhole-free Ti foils as entrance window any longer due their thickness. Thinner entrance windows with sufficient mechanical stability, also when cooling the system down to 40 K, and not jeopardizing the high cleanliness need to be identified and tested.

2.4 Resonance ionization laser spectroscopy at SHIP

A complementary approach for studying atomic and nuclear properties of the heaviest elements produced at the SHIP velocity filter uses the technique of resonance ionization spectroscopy (RIS). Laser spectroscopy in general is a versatile tool to unveil the atomic structure of an element, which in turn can be used to access properties of the nucleus [87, 88]. Advancing techniques developed at the University of Mainz [89] for the laser spectroscopy investigation of elements heavier than fermium was accomplished, allowing for both shedding light on the atomic and on the nuclear structure of these heavy nuclides. In this section, a short introduction to the technique of resonance ionization spectroscopy is followed by a summary of the pioneering laser spectroscopic experiments on nobelium ($Z = 102$) performed at GSI, Darmstadt. Finally, an outlook to future activities will be given.

2.4.1 Resonance ionization spectroscopy

Laser spectroscopy uses optical transitions in the electronic shell of an atom to elevate electrons into orbitals with a higher energy. In RIS, the excited electron is removed from the atom by applying an additional laser excitation step with high photon fluxes and a photon energy sufficient to excite the electron above the first ionization potential (IP) [90, 91]. This photo-ionization of the atom finally results in an ion which can be manipulated by electric fields and detected more efficiently. With this technique, properties of atomic transitions such as excitation energies and lifetimes can be measured, characterizing the element's electronic structure. From a measurement of the hyperfine-structure (HFS) splittings for isotopes with a non-zero nuclear spin nuclear properties such as the nuclear spin, the magnetic dipole moment, and the quadrupole moment can be obtained [88]. A more general overview of different laser spectroscopy techniques applied to heavy elements is given in a recent review [92]. A few neutron-rich isotopes of the heavy actinide elements einsteinium (Es, $Z = 99$) and

fermium (Fm, $Z = 100$) can still be produced in weighable amounts of few picograms to nanograms in nuclear reactors by successive neutron captures and delayed β decays [93]. This allows some off-line measurements, but due to the limited sample sizes the information on the atomic structure is still scarce [92, 94, 95]. For the heavier transfermium elements ($Z > 100$), no atomic information was available experimentally prior to the investigations in nobelium (No, $Z = 102$) at SHIP [96], as these elements can only be produced in single-atom-at-a-time quantities in fusion reactions using intense heavy-ion beams from accelerators. Due to a lack of stable isotopes and the low production rates, theoretical predictions of the atomic structure are essential to guide any experimental search for atomic levels. These calculations are complicated by strong electron-electron correlations in these heavy systems and by the relativistic effects arising from the strong Coulomb force at the nucleus [97]. Having said that, the accuracy of the applied theoretical atomic models can be probed by the experimental determination of atomic-level energies and other atomic properties.

Once an atomic transition is found, it can be studied for different isotopes of the same element [88]. The obtained resonance signal will feature an isotope shift arising from a change in the nuclear volume and mass, while the interaction of the angular momentum J of the electron with a non-zero nuclear spin $I \neq 0$ results in a HFS splitting given by

$$\Delta E_{\text{HFS}} = A\frac{C}{2} + B\frac{(3/4)C(C+1) - I(I+1)J(J+1)}{2I(2I-1)J(2J-1)} \tag{4}$$

$$\text{with } C = F(F+1) - I(I+1) - J(J+1),$$

$$A = \mu\frac{B_e(0)}{IJ}, \quad \text{and } B = eQ_s\left\langle\frac{\partial^2 V}{\partial z^2}\right\rangle_0. \tag{5}$$

This splitting results in levels with a total angular momentum F where the separation of the individual levels is determined by the hyperfine parameters A and B. These hyperfine parameters are linked to the interaction of the magnetic field induced by the electrons at the position of the nucleus, $B_e(0)$, with the nuclear magnetic moment μ and to the electric-field gradient at the nucleus, $\left\langle\frac{\delta^2 V}{\delta z^2}\right\rangle_0$, interacting with the spectroscopic quadrupole moment Q_s of the nucleus. The electronic part is typically inferred from HFS measurements on reference isotopes with known nuclear moments enabling the determination of nuclear moments for exotic isotopes [88]. Unfortunately, this does not work for the heaviest elements where a reference isotope with an independently determined nuclear moment does not exist. Therefore, atomic calculations of $B_e(0)$ and $\left\langle\frac{\delta^2 V}{\delta z^2}\right\rangle_0$ are required for the extraction of nuclear properties. Also, calculated mass shift and field-shift factors allow us to derive the changes of the mean-square charge radii from measured isotope shifts.

2.4.2 The RADRIS experiment at GSI

The ER from the fusion reaction have typical energies of several 10 MeV (e.g. about 37 MeV in the case of ^{254}No) with an energy spread of several MeV rendering any direct laser spectroscopy impossible. Stopping and thermalization of the fusion products in a buffer-gas environment is therefore mandatory before performing laser spectroscopy.
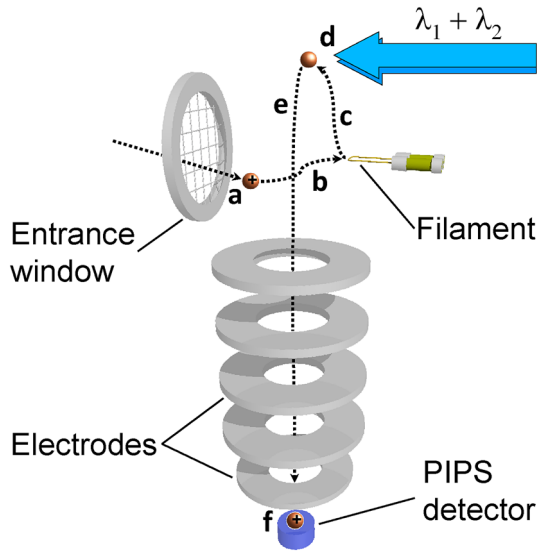
Fig. 7 Principle of the RADRIS technique. The incoming fusion products are thermalized in buffer gas and then accumulated on the catcher filament. From there they are re-evaporated and the released neutral atoms are excited by two-step photoionization using two laser beams of different wavelengths. Photo-ionized fusion products are guided to a Passivated Implanted Planar Silicon (PIPS) for a selective detection of their radioactive decay

At SHIP, the so-called Radiation Detected RIS (RADRIS) method was applied successfully for laser spectroscopy of the transfermium element nobelium ($Z = 102$). This technique has originally been developed at University of Mainz, based on the experience with on-line laser spectroscopy on fission isomers in americium (Am, $Z = 95$) [89]. Here, the fraction of the incoming radionuclides, which was neutralized during stopping in argon buffer gas, was probed by laser resonance ionization spectroscopy and detected by their radioactive decay.

As the main fraction of stopped particles remains in an ionic state, a metallic filament was introduced to use electric fields for the collection of ions and subsequent thermal reevaporation of neutral species [98]. In this configuration, the filament material is crucial as a thermal desorption in combination with a low surface-ion yield is essential to the experiment. This has therefore to be verified and optimized for each element under investigation. The development of the RADRIS technique was continued at GSI, Darmstadt [23, 99, 100] and tantalum was found to be a suitable filament material for nobelium in off-line studies with the homologue element ytterbium, which features a similar electron configuration. The RADRIS setup is sketched together with the measurement procedure in Fig. 7. The incoming fusion products are slowed down in a buffer-gas volume and the stopped ions are guided by an electric field to a filament, a 125-μm thick tantalum wire for the nobelium experiments.

After a collection time, the primary beam is stopped and the filament is heated (to around 1050 °C for nobelium) to release the captured ions as neutral atoms. The evaporated atoms are probed by laser light and in case the photon energy matches an optical transition converted to a photo-ion by the very intense second laser. Due to the

buffer gas in the cell the atom velocity is reduced, confining the area to be illuminated with the laser light as well as enabling the use of laser light with high pulse energy, a pre-requisite for an efficient photo-ionization. The tunable laser light is provided by excimer-pumped dye lasers while the ionization laser light originates directly from an excimer laser. Both lasers have a repetition rate of 100 Hz, which is suitable for typical drift times of the atoms in the buffer gas on the order of few milliseconds. The created photo-ions are guided to a silicon detector where their characteristic α-decay energy is detected, which in addition to the high efficiency of the setup ensures a high selectivity in the detection. The RADRIS method can be applied to α-decaying nuclides with half-lives of about 1–10,000 s. Depending on the decay mode of the collected radionuclide, the decay daughters remain on the filament and become accessible for laser spectroscopy as well. This opens up the access to nuclides that are difficult or impossible to produce directly. Proof-of-principle experiments for this approach have already been performed at the GSI. For example, the electron capture decay of ^{255}Lr has been exploited to produce ^{255}No and measure its hyperfine structure with RADRIS.

2.4.3 Recent results from laser spectroscopy

The RADRIS setup was coupled to SHIP for the atomic level search in nobelium. At the time of the first experiment was started, different theoretical predictions existed [101–105]. They all predicted a strong $^1S_0 \rightarrow {}^1P_1$ ground-state transition with an excitation energy of about 30,000 cm^{-1}. However, due to the uncertainty of these predictions, a span of more then 1200 cm^{-1} corresponding to more than 3,000 scan steps had to be covered. Therefore, several beamtimes were required until finally in 2016 a first optical transition in nobelium was observed and characterized [97]. Besides the determination of the excitation energy to 29,961.45 cm^{-1} the saturation of this transition, measured with varying laser intensities, revealed a transition strength of $4.2 \cdot 10^8$ s^{-1}. The energy as well as the transition strength match very well with the predictions for the $^1S_0 \rightarrow {}^1P_1$ ground-state transition [102, 105], indicating that the strong electron correlations can be calculated at a high precision for heavy systems with nearly closed atomic shells. The lifetime of the excited level was additionally probed by varying the time delay between the first laser excitation pulse and the ionizing, second laser excitation pulse. This measurement revealed a delayed ionization for delay times much longer than the expected lifetime of about 2 ns for the $^1P_1$ state obtained from the transition strength. The same behavior was observed in off-line investigations using stable Yb isotopes. Varying the buffer gas pressure revealed that the ion rate for large delays between the two laser pulses strongly increased with an increasing buffer-gas pressure.

These observations match with a strong population transfer from quenching by gas collisions to lower, but close-by, atomic levels with a sufficiently long lifetime enabling a delayed ionization. Such states are known to exist from theoretical predictions of the ^3D states. This assumption was verified by addressing Rydberg levels which are only accessible from certain atomic levels giving a unique fingerprint [106].

In a similar arrangement, the shift of Rydberg levels in Yb in the presence of a buffer-gas environment was studied off-line quantifying the resulting shift in the extraction of the IP [107]. With these findings and the on-line measurements of Ryd-
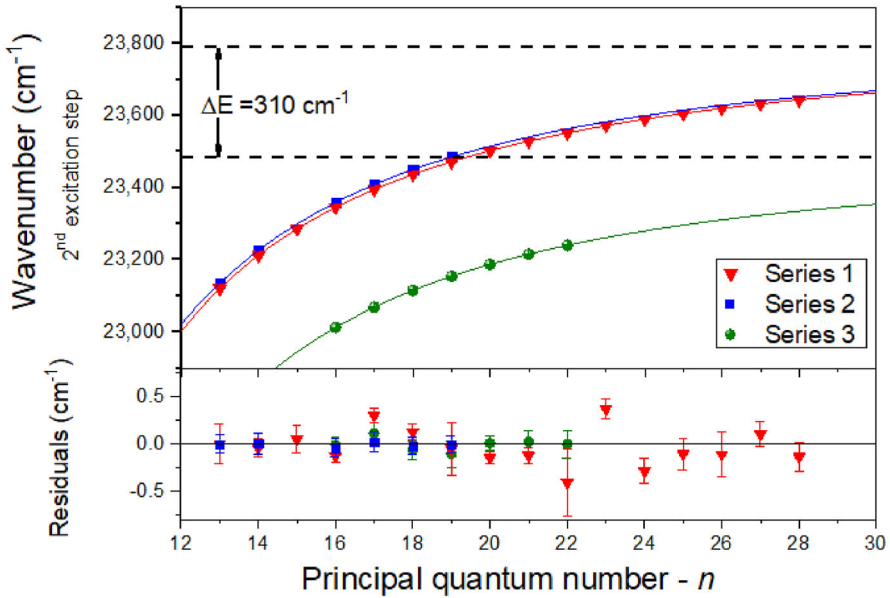
Fig. 8 Convergence of the observed Rydberg levels in nobelium. The curve indicates a best fit of a Rydberg series convergence to the data. The observed three series clearly converge to two different limits as a result of buffer-gas quenching. For details see text and ref. [108]. Reprinted figure with permission from Chhetri et al. [108]

berg levels in nobelium, is was possible to extract the first ionization potential of nobelium to 6.62621(5) eV [108]. This value is in very good agreement with theoretical predictions [102] and also matches recent measurements with a lower accuracy from surface-ionization yields at different temperatures reported by Sato et al. [109]. The observed Rydberg levels belonged to distinct Rydberg series converging to different limits as shown in Fig. 8. This behavior enabled determining the energy difference of the optically excited level and the atomic state to which the electron population quenches to be $310 \, cm^{-1}$, while comparison to literature suggest this level to have a $^3D_3$ configuration [108].

Besides probing the atomic structure of nobelium, which revealed more than 30 atomic levels to date, different isotopes were investigated as shown in Fig. 9. In addition, the resonance of the investigated $^1S_0 \rightarrow \, ^1P_1$ ground-state transition was measured for the isotopes ^{252,253,254}No. The isotope shift of the individual resonances reflects the change in nuclear volume determined by the mean-square charge radius [88]. The resonance spectrum of the isotope ^{253}No furthermore shows a hyperfine structure splitting originating from the non-zero nuclear spin as discussed in Sect. 2.4. From the angular momentum of the atomic ground state $J_{GS} = 0$, the excited state $J_{ES} = 1$ and the nuclear spin of $I_{253-No} = 9/2$ a total of three atomic transitions are expected, which were not fully resolved in the measurements. Nonetheless, the fit to the data is in agreement with this spin assignment. To infer nuclear properties from the measured hyperfine splitting, the atomic properties have to be known, *c.f.* Eq. 4. As no reference isotope is available for a relative measurement, atomic theory pro-
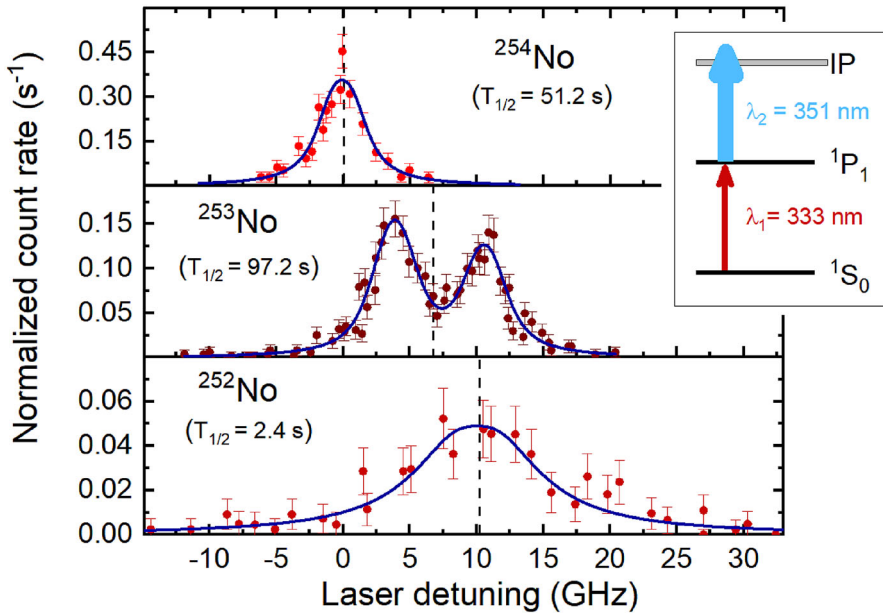
Fig. 9 Measured spectra of the $^1S_0 \rightarrow {}^1P_1$ transition in the nobelium isotopes $^{252-254}$No. In ^{252}No the laser was operated at a larger bandwidth for an improved efficiency. The solid lines show the best fit to the experimental data. Figure adapted from Ref.[110]. Reprinted figure with permission from Raeder et al. [110]

vided the atomic coupling factors for the hyperfine structure as well as for the isotope shift, enabling the determination of nuclear moments and changes in the mean-square charge radii [110].

2.4.4 Future prospects for laser spectroscopy

Besides the already discussed isotopes ^{252,253,254}No, which have already been investigated experimentally, the isotopes ^{251,255}No are in reach with the RADRIS technique. Their half-lives and their production cross sections are summarized in Table 2. In this consideration only cold-fusion reactions with lead and bismuth targets have been considered. The production of more neutron-rich nobelium isotopes is possible, using more asymmetric reactions. As already discussed in Sect. 2.3.2, the SHIP transmission is very low for very asymmetric reactions of light projectiles (such as C, O) and actinide targets (such as Pu and Cm). For ^{255}No an indirect production via the electron capture (EC) branch of ^{255}Lr is beneficial as the direct production via the 1 n-evaporation channel in the ^{48}Ca + ^{208}Pb reaction always produces the isotope ^{254}No in the 2 n-evaporation channel with a similar cross section [33]. Both isotopes, ^{255}No and ^{254}No, have very close-lying α-decay energies around 8.10 MeV [79], reducing the selectivity from decay detection in this particular case. Some experimental data for ^{255}No has already been taken and an estimate of the obtained effective cross-section is stated in Table 2 while the data is still under evaluation.

Table 2 Production schemes and fusion-evaporation cross sections for isotopes of interest in the RADRIS measurements

Nuclide	Half-life (s)	Reaction	Cross section (nb)
^{254}No	51.2	^{48}Ca(^{208}Pb, 2n)	2100 [111]
^{253}No	97.2	^{48}Ca(^{207}Pb, 2n)	1300 [111]
^{252}No	2.44	^{48}Ca(^{206}Pb, 2n)	500 [111]
^{255}No	211.2	^{48}Ca(^{209}Bi, 2n)→EC	40–60 (eff.)
^{251}No	0.8	^{48}Ca(^{206}Pb, 3n)	30 [111]
^{254}Lr	18.1	^{48}Ca(^{209}Bi, 3n)	22 [112]
^{255}Lr	31.1	^{48}Ca(^{209}Bi, 2n)	200 [113]
^{256}Lr	27.0	^{48}Ca(^{209}Bi, 1n)	60 [33]

The half-lives were taken from the Evaluated Nuclear Structure Data Files [79]. For the decay-assisted spectroscopy of ^{255}No, i.e., the production by electron-capture from directly produced ^{255}Lr, the effective (eff.) cross-section is estimated

The second isotope in reach is ^{251}No with a cross section of about 30 nb, about a factor of ten lower than in the case of ^{252}No. The short half-life of only 0.8 s is at the edge for the application of the RADRIS technique as the sequential collection and evaporation cycle is prone to decay losses and a fast switching is mandatory. A low-lying isomer with slightly longer half-life (1.02 s [79]) additionally complicates the measurements.

Besides extending the isotopic chain on both sides of the $N = 152$ shell by measuring further nobelium isotopes, the concept of laser spectroscopy on decay-daughter nuclei can be used to access additional nuclides that are inaccessible (of unfavorable) in a direct production scheme. The α-decay of nobelium, e.g., leads to fermium isotopes that can be probed with laser spectroscopy in an adapted cycle allowing for breeding these nuclei on the filament. For fermium some atomic levels were already reported [94, 114]. In this context, the scan for atomic levels becomes unnecessary. In this concept new isotopes and elements will become available with a reduced efficiency due to the applied cycle and losses from recoils pushed into the filament material.

An obvious next step is the application of the RADRIS techniques to search for atomic levels in the next heavier element, lawrencium (Lr, $Z = 103$). The cross sections for the production of different Lr isotopes are shown in Table 2. However, even the highest cross section for the production of ^{255}Lr is an order of magnitude lower compared to ^{254}No. Nevertheless, the determination of atomic properties in lawrencium is of particular interest as the atomic ground state configuration is predicted to be 7s^2 7p ^{2}P$^\circ_{1/2}$, and thus different from its iso-electronic homologue, lutetium, which has a 6s^2 5d ^{2}D$_{3/2}$ ground-state configuration. For the lawrencium atom several predictions for atomic levels are available [105, 115–118] predicting two suitable strong ground-state transitions located around 20 400 cm^{-1} and around 28 400 cm^{-1} in the visible and the ultraviolet spectral range, respectively.

As discussed in Sect. 2.4.2 the desorption of collected fusion products from the filament is a crucial step in the RADRIS technique. As the 7s-shell of the atomic shell
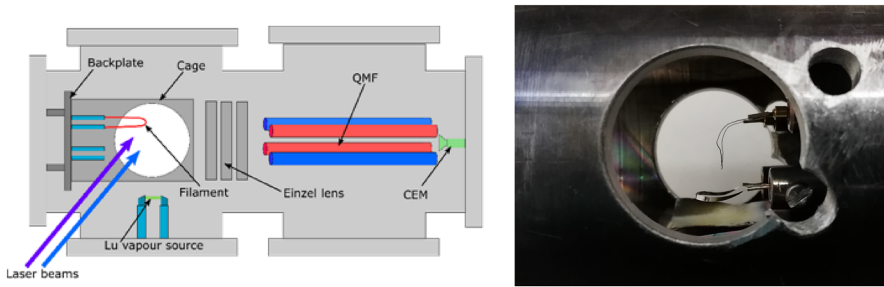
Fig. 10 (Left) Schematic layout of the off-line setup for studying the desorption behavior of lutetium from different filament materials. Details see text. (Right) A picture of two different hafnium filaments after heating to the desired desorption temperature. The upper filament is a $100\,\mu$m-thick wire which deformed strongly, whereas the lower strip-type filament with dimensions of $25\,\mu$m$\times 1$ mm only barely deforms. The picture was provided by the courtesy of J. Warbinek

is fully occupied in nobelium, the atomic spectrum of lawrencium features p- and d-electronic orbitals leading to a higher desorption temperature due to an increasing refractory character of the transition metals along the actinide series. The IP of lawrencium ($E_{IP} =4.96$ eV) [109, 119] is significantly lower compared to nobelium, giving rise to an increased surface ionization fraction. The desorption was therefore studied off-line in the homologue element, lutetium, in a dedicated setup as sketched in the left part of Fig. 10. This setup consisted of a vapor source for evaporating Lu onto the filament to be tested and thus, the collection and evaporation cycle can be simulated with a filament analogue to the one used in the on-line RADRIS technique [23]. Resonantly tuned laser light is overlapped with the cloud of evaporated atoms to probe the neutral fraction by resonant laser ionization. The ions are guided through a quadrupole mass filter for selection according to mass-to-charge ratio and detected using a channel electron multiplier (CEM) in single ion counting. A detailed description can be found in [120]. This setup allowed the study of the desorption behavior as well as to monitor the surface-ion contribution for different temperatures and materials. From the different materials tested, hafnium turned out to be the most suitable material featuring a surface-ion yield, which was reduced by a factor of at least ten compared to tantalum, but required a desorption temperature of 1800 °C. A problem arose from the mechanical stability of the filament at high temperatures. The typical geometry of a 125 μm-thick wire as used with tantalum in the nobelium spectroscopy experiment turned out to be mechanically unstable. This can be seen in the right part of Fig. 10. The upper filament is a 125 μm-thick Hf wire heated to the desorption temperature of Lu and clearly is deformed. The solution was a change in the filament geometry to a 25 μm thick and 1 mm wide strip geometry as shown in the lower filament position of Fig. 10. This strip filament was also heated to the desorption temperature of Lu and showed only a minor deformation not hampering the experiment. With Hf as filament material and the optimized geometry a level search in lawrencium with RADRIS is now feasible.
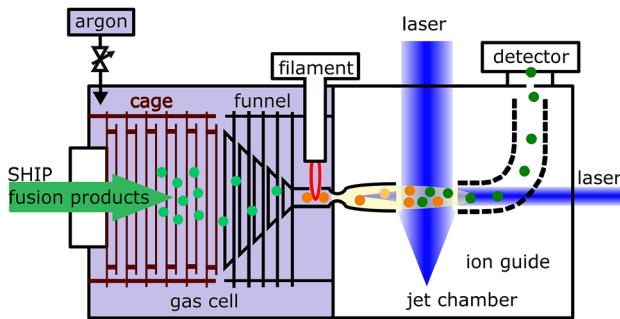
Fig. 11 Schematic setup of the apparatus for laser spectroscopy in the gas jet at GSI. The fusion products are stopped in the gas cell filled with about 50–80 mbar argon gas. The cage and the funnel electrode structures guide the ions to the filament. The filament is heated for neutralization and desorption of neutral atoms which are transported by the gas flow and extracted in a gas jet for RIS

2.4.5 A gas-jet setup at GSI for improved spectral resolution

The spectral resolution in the RADRIS technique is ultimately limited by pressure broadening of the atomic lines in the buffer-gas environment, where the laser spectroscopy is performed. A new technique for improved spectral resolution proposed by Kudryavtsev et al. [121] is the laser ionization in a well-collimated gas jet effusing out of the gas cell used for stopping of evaporation residues. The lower temperatures and gas densities in a gas jet enable laser spectroscopy with improved resolution. The crucial part is the de Laval nozzle needed for forming a well-collimated gas jet. This is required as the gas velocities in such a jet are about 550 m/s for argon as buffer gas. Therefore, an extended interaction volume of the gas jet with the laser light is required in addition to a narrow-bandwidth and high-repetition-rate laser system [122] for maximum efficiency. The technique was successfully applied on-line to neutron-deficient actinium (Ac, $Z = 89$) isotopes at the Leuven ISOL (Isotope Separator OnLine) separator with a tenfold improved resolution compared to in-gas-cell laser spectroscopy [123]. A continuous improvement of the technique including an efficient and thorough nozzle characterization optimized for laser spectroscopy of the heaviest elements is carried out in Leuven [124–127].

A dedicated gas-jet setup for laser spectroscopy of the heaviest elements at GSI is presently commissioned [128]. It combines the neutralization on a heated filament from the RADRIS technique with the laser spectroscopy in the effusing gas jet. A schematic layout of the system is shown in Fig. 11. The incoming recoil ions are stopped in argon buffer gas and guided by electric fields to a heated filament. On this filament, the ions neutralize and neutral atoms are transported further by the gas flow to the exit nozzle. The converging-diverging nozzle features a de Laval shape forming a well-collimated gas jet for high-resolution laser spectroscopy. A high-repetition-rate (10 kHz) dye-laser system is used for resonant excitation and ionization. The created photo ions are extracted and transported by a radio frequency quadrupole (RFQ) ion guide which is bend by 90° to enable a longitudinal access of the laser light to the gas jet. The ions are finally detected by a CEM, albeit a silicon detector for a radiation-

assisted detection is feasible as well. The achievable resolution is projected to be well below 400 MHz (FWHM) constituting an improvement by about one order of magnitude compared to the RADRIS technique. Such a resolution will benefit future experiments in particular the extraction of nuclear spins and electromagnetic moments from the HFS splitting. In addition, the setup allows a continuous operation giving access to both, much longer-lived nuclei by ion counting, and also to shorter-lived nuclei by minimizing decay losses that occur in the RADRIS technique. One case that can be tackled with the new setup is the 8^- K-isomer in ^{254}No with a half-life of 266 ms [79]. A laser spectroscopy measurement of the magnetic moment will enable the unambiguous determination of the configuration of this isomer that is still not unambiguously assigned as there are two different (quasi-particle) configurations that can form an 8^- K-state in ^{254}No [129].

2.5 Alpha–Gamma spectroscopy

An atomic nucleus consists of a number of nucleons (protons, neutrons) which interact via a strong attractive short-range force and the long range disruptive Coulomb force. The stability of a nucleus is thus governed by the ratio of the strength of these basic interactions. This feature becomes specifically important in regions of 'extreme' proton to neutron ratios (very neutron deficient or neutron-rich nuclei) and for the heaviest nuclei. In these cases, subtle details in the description of the strong force become important and will not only determine the location and the strength of the next spherical proton and neutron shells above ^{208}Pb ($Z = 82$, $N = 126$), but also the properties and stability of the heaviest nuclei in general. Under these considerations an extensive program to investigate properties of heaviest nuclei was started at SHIP [82, 83, 112, 130–140]. The main objectives of these experiments were: (a) study of decay properties, i.e. α decay, electron capture (EC), spontaneous fission; (b) identification of excited states, measuring the excitation energies and determining their spins and parities; (c) investigation of isomeric states with specific emphasis on K-isomers. From previous studies it was known, that excited levels show some systematic trends (with respect to excitation energies, spins and parities) along the isotone lines in even-Z odd-mass nuclei and along the isotope lines in odd-Z odd-mass nuclei. This feature has been consequently followed in experiments at SHIP for two decades, with systematic studies of even-Z nuclei along the the $N = 147$ to $N = 153$ isotone lines and along the isotope lines in odd-mass nuclei with $Z = 101$ and to lower extent $Z = 103$, 105. Specific nuclei to be investigated, however, were mostly selected with respect to known or expected production cross sections to obtain a maximum of information within limited irradiation times.

2.5.1 Detector setup at SHIP

Up to 2014, a detector system consisting of a 16-strip Si-'stop detector' (size 80 × 35 mm^2) surrounded upstream by a 'box' of six Si-strip detectors of equal size as the 'stop detector' was used in the focal plane of SHIP [28]. The strips were position sensitive in vertical direction, which was achieved by charge division. To discriminate
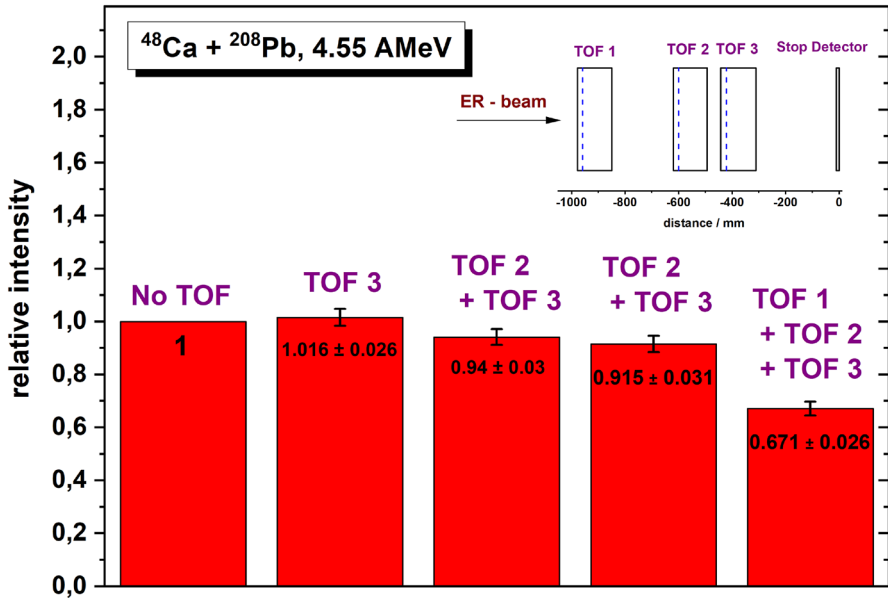
Fig. 12 Transmission reduction for ^{254}No residues due to scattering in the TOF foils

signals from implantation e.g., ER, scattered projectiles or decays e.g., α particles, SF events and light particles e.g., protons, α particles, deuterons produced in nuclear reactions with the target or backing material that may pass SHIP, another Si - detector of the same type and size was mounted behind the 'stop detector'. In front of the detector box, three time-of-flight (ToF) detectors were installed [141]. Due to scattering of the ER in the TOF-detector foils causing losses in transmission, usually only two detectors were used. This influence is shown in Fig. 12 for the production of ^{254}No in the reaction ^{208}Pb(^{48}Ca,2n)^{254}No.

For γ spectroscopy, a Ge-clover detector was mounted in close geometry behind the 'stop detector'. Gamma rays emitted in prompt or delayed (within a time window Δt(particle-γ) $\leq 5\,\mu$s) coincidence with particle registration in the 'stop' or 'box' detector were measured using a Ge detector. Two types of Ge detectors were used: either a clover detector of VEGA type [142] consisting of four crystals, each of 70 mm diameter and 140 mm length, which were shaped and assembled to form a block of $(124 \times 124 \times 140)\,\text{mm}^3$, or a smaller Clover detector consisting of four crystals, each of (50–55) mm diameter and 70 mm length, shaped and assembled to form a block of $(102\times102\times70)\,\text{mm}^3$ ('SHIP Clover'). Time differences between particles and γ events within the above mentioned time window of 5 μs, determined by the data acquisition system, were measured using a TAC with a resolution of $\Delta t = 1\,\mu$s (FWHM) for the 'prompt' peak.

Detector pulses fed to ADCs started a coincidence time of usually 5 μs; after that time the ADCs were blocked and conversion and readout started, taking typically about 15 μs, which defined the deadtime of the system, during which incoming signals were not recorded.

Although the detector set-up was operated successfully for about 20 years, two severe disadvantages became evident. First, the above mentioned deadtime did not allow for an (effective) spectroscopy of short-lives isotopes or nuclear states (isomers). Second, the lack in sensitivity of the method to determine the position by charge division. Signals for low-energy particles such as CE and escaping α particles became quite low, often smaller than the threshold of the ADCs, ranging between 20 mV (under optimum conditions, i.e. no electronic noise and detectors of high quality) and 200 mV, if detectors had already suffered from radiation damages. Thus, often no or only one position signal was recorded. In addition, the position resolution suffered from non-linearities of the amplifiers in the range of low signals (< 500 mV). The position resolution for low-energy events ('escape' α particles and CE) was ≥ 1 mm (FWHM), whereas for α particles in the range 6–10 MeV it was ≈ 0.3 mm (FWHM).

Therefore the detector system was replaced by the fully digitized setup COMPASS that uses pixelized detectors and has been described in detail along with the results of first performance experiments elsewhere [19]. Here we will summarize the main features.

The arrangement consists of a double-sided silicon-strip detector (DSSD) of 60×60 mm^2 in the focal plane. It has on each side 60 strips either in vertical or horizontal direction. Four single-sided silicon strip detectors (SSSD) of 60×60 mm^2 with 32 strips each forming a semi-box are arranged in front of the focal plane detector. The frames serving as holders for the silicon detectors are connected to copper tubes used for cooling with ethanol reaching typical temperatures of 263–268 K. The arrangement is placed inside an aluminum end cap having on each side circular windows of 80 mm diameter and a thickness of 1.5 mm to minimize absorption of low-energy photons.

For signal processing three options are available:

1. a pure analogue solution: charge-sensitive preamplifiers, pulse-shaping and peak-sensing ADCs
2. a digital solution: the preamplifier signals are fed to FEBEX3 digitizers [143], at the heart of which are pipelining ADCs with 12 bit (14 bit) data range and 60 MHz (50 MHz) sampling rate
3. the use of ASIC–APFEL (**A**SIC for **P**ANDA **F**ront-**E**nd **EL**ectronics) chips for detector read-out [144] placed inside the vacuum chamber of the detector box.

For the present purpose, a version of the signal processing was produced providing two input channels equipped with two different output channels. One of the latter had a switchable amplification factor of 16/32 with respect to the other one. The width of the output signals, which were fed to FEBEX3 modules, was ≈ 300 ns.

For energy extraction a fast trapezoidal filter is used [145].

2.5.2 Decay study of ^{258}Db

In recent experiments at SHIP investigations of ^{247}Md and ^{255,257}Rf were continued. However, special focus was given to a decay study of ^{258}Db to solve two long-standing problems. First of all, to prove the existence of two long-lived states in ^{258}Db and its α-decay daughter ^{254}Lr, both decaying by α emission and/or by electron capture (EC). On the other hand, a direct proof of the EC decay of ^{258}Db could be obtained by

measuring the K X-rays emitted during the EC process in delayed coincidence with spontaneous fission of the EC-daughter ^{258}Rf.

^{258}Db was first observed in an irradiation of ^{209}Bi with ^{50}Ti in 1981 [146, 147]. In this experiment besides α decay of ^{258}Db also spontaneous fission with the same half-life as the α activity ($T_{1/2} \approx 4$ s) was observed and attributed to the decay of the same isotope. As ^{258}Db is an odd-odd nucleus it was not expected to undergo spontaneous fission itself. It was rather assumed that this isotope undergoes EC decay and fission of the EC-daughter ^{258}Rf, a known SF activity of ≈ 11 ms half-life, was observed. In an experiment performed in 1982, it was attempted to prove this assumption by measuring the K X-rays emitted during the conversion electron (CE)-emission in delayed coincidence with SF of ^{258}Rf. The result of this study is shown in the upper panel of Fig. 13 [148] which was obviously not conclusive and therefore not published. In 2014, a successful measurement was eventually performed [149] and the photon spectra measured in delayed coincidence with fission events are shown in the lower panel of Fig. 13. Part of the SF events were measured in delayed coincidence with CE, i.e., we observed event sequences starting with implantation of an evaporation residue, followed by detection of a CE and terminated by a SF event ((ER, ^{258}Db)–CE–SF (^{258}Rf)). It was realized that (a) the fission events in delayed coincidence with CE had a longer half-life (4.4 ± 1.0 s) than those without CE (3.6 ± 0.3 s); although not completely unambiguous due to overlapping error bars this was seen as a hint for the existence of two long-lived states in ^{258}Db already suggested by a previous α-decay study [82]; (b) EC decay of ^{258}Db also populated two short-lived isomeric states in ^{258}Rf with half-lives of 15 ± 10 μs and $2.4^{+2.4}_{-0.8}$ ms. The decay scheme is sketched in Fig. 14.

The existence of two long-lived states in ^{258}Db was finally proven by the α-γ-decay studies [81], which resulted also in the existence of two long-lived isomeric states in the daughter nucleus, ^{254}Lr, and the granddaughter, ^{250}Md. The isomeric state in ^{254}Lr was meanwhile also confirmed by direct mass measurements with SHIPTRAP that will be published in a forthcoming paper.

2.5.3 Decay study of ^{257}Rf

The isotope ^{257}Rf was first observed by Ghiorso et al. [150] in the reaction ^{249}Cf(^{12}C,4n)^{257}Rf. They observed a complex α spectrum with energies in the range (8.5–9.0) MeV and measured a half-life of $T_{1/2} = (4.5\pm1.0)$ s. A couple of years later the results of Ghiorso et al. were confirmed by Bemis et al. [151], using the same reaction. In this experiment, photons were additionally measured in prompt and in delayed coincidence with K X-rays. Four groups of photon events were observed, which fitted to the expected $K_{\alpha 1}$, $K_{\alpha 2}$, $K_{\beta'_1}$, and $K_{\beta'_2}$ X-ray energies of nobelium. It was thus the first direct Z-identification of a transactinide element. As some of the X-ray events were observed in delayed coincidence with α particles, Bemis et al. concluded that (at least) part of α decays of ^{257}Rf populate an isomeric level in ^{253}No. They attributed a half-life of $T_{1/2} = (31.1\pm4.1)$ μs and an excitation energy $E^* \approx 300$ keV to the isomer.

At SHIP, this isotope was produced in two ways. A direct production was obtained via the reaction ^{208}Pb(^{50}Ti,n)^{257}Rf [152, 153], while it can be studied by an indirect production from the α decay of ^{261}Sg, directly produced in the reaction
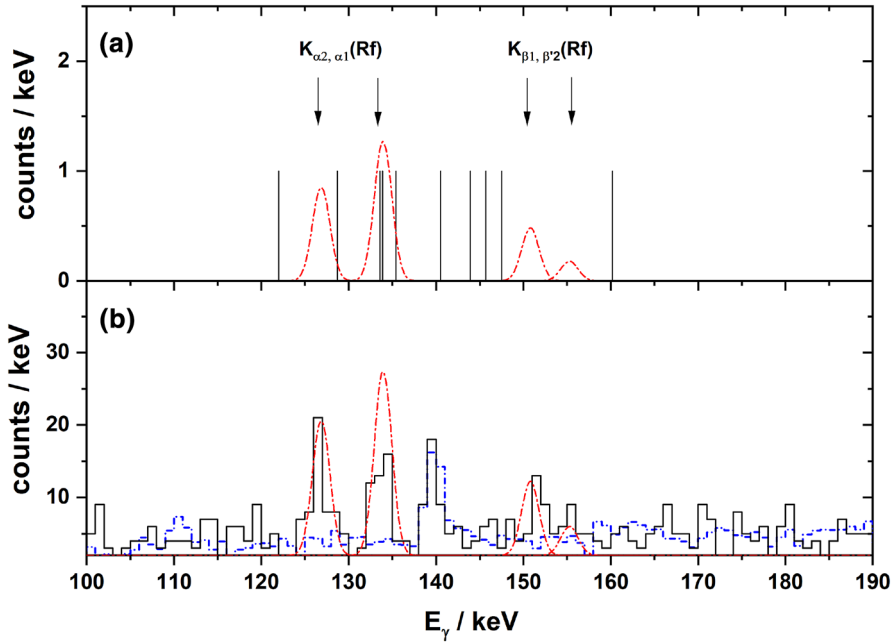
Fig. 13 Spectra of photons observed in delayed coincidences with fission events of ^{258}Rf within Δt(photon-SF)$\leq$ 30 ms; **a** experiment 1982; **b** experiment 2014. The red dashed-dotted lines mark the calculated energies of the K$_\alpha$, K$_\beta$ X-rays, using a detector resolution of 1.5 kev (FWHM). The blue dashed-dotted line represents the gamma background without beam, scaled to the 140 keV background-line, which was not assigned
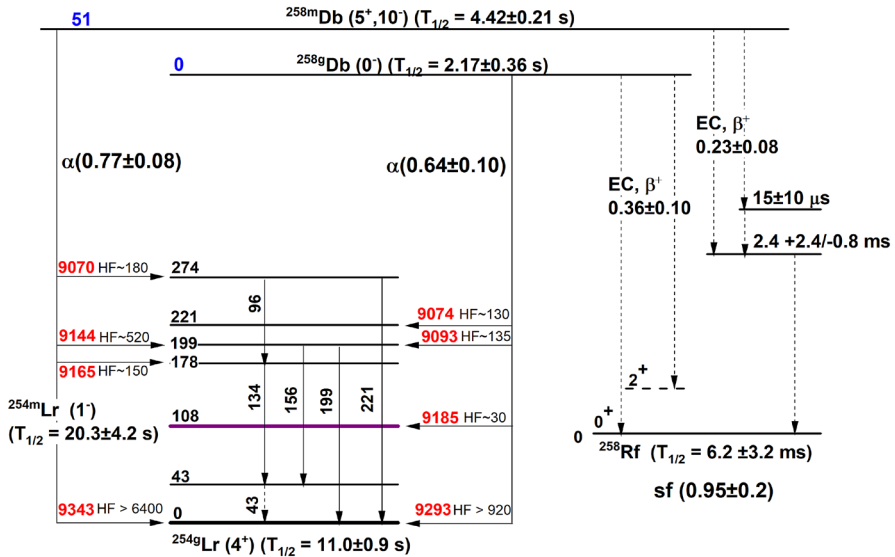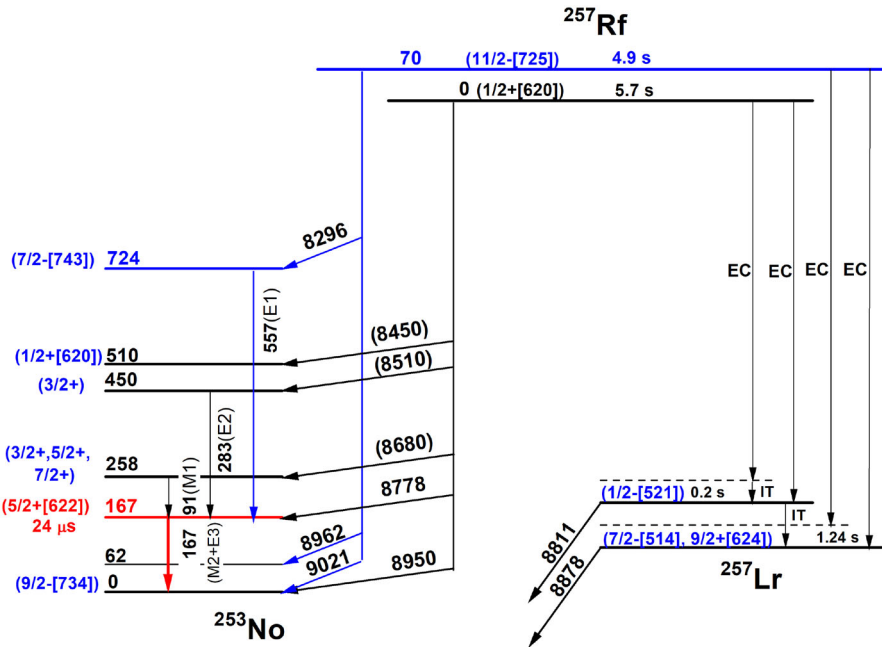

Fig. 14 Decay scheme of ^{258}Db

Fig. 15 Decay scheme of ^{257}Rf

^{208}Pb(^{54}Cr,n)^{261}Sg [83, 153]. It was shown that the two lines of highest energy are missing in the indirect production. This led to the assumption of a low-lying isomeric state in ^{257}Rf with a tentative configuration $11/2^-$[725], that was populated in the direct production, but not by decay of ^{261}Sg. In a follow-up study the energy of this isomeric state was settled at $E^* = 70$ keV, while the isomeric state in ^{253}No with a tentative configuration $5/2^+$[622] was located at $E^* = 167$ keV [83].

Within the experiment on the decay properties of ^{258}Db also a relatively short irradiation (ca. 24 h) of ^{208}Pb with ^{50}Ti to produce ^{257}Rf was performed. As a new result we observed a γ transition of 577 keV (2 events) in coincidence with α particles of 8296 keV, which was attributed to the decay of the $11/2^-$[725] isomer into a—so far not reported—$7/2^-$[743]-state in ^{253}No decaying into the $5/2^+$[622] isomeric state [154].

Specific emphasis was laid on the investigation of the EC decay of ^{257}Rf. For this purpose also the data from a previous study [83] were reanalyzed to detect possible differences in the EC decay of the ground state and the isomeric state. It was shown that in the direct production, where about 2/3 of the observed α decays stem from the isomer, a ^{257}Lr line of 8878 keV was observed, as also in the decay of ^{261}Db [83, 155], while in the production via decay of ^{261}Sg a significant line at 8811 keV was recorded [156]. A careful analysis resulted in half-lives of $T_{1/2} = 0.20^{+0.16}_{-0.06}$ s for the 8811 keV transition and $T_{1/2} = 1.24^{+0.85}_{-0.36}$ s for the 8878 keV one, which clearly proved the existence of two states in ^{257}Lr decaying by α emission. As the latter was observed in the direct production it was attributed to a high spin state, while the 8811 keV

transition was attributed to the decay of a low spin state. This observation was not surprising as a similar behavior was encountered also in the lighter odd-mass isotopes [253]Lr [130] and [255]Lr [112, 157]. The (partial) decay scheme for [257]Rf deduced from the recent SHIP experiments is shown in Fig. 15.

2.5.4 Isomeric states in [255]Rf

After identification of a K-isomeric state in [270]Ds living longer than the ground-state [158] and the first γ spectroscopy investigations of K-isomers in [254]No [129, 159] investigation of K-isomers came into the focus of nuclear spectroscopy of SHE. At SHIP, new K-isomers or candidates for K-isomers were identified in [251]No [134], [252]No [135, 160], [253]No [138, 161], [255]No [137], [266]Hs [162], and [258]Rf [149].

Within the experiment on the investigation of [258]Db we also performed a short irradiation (≈ 40 h) of [207]Pb with [50]Ti to produce [255]Rf. Main focus was to measure the total kinetic energy (<TKE>) of SF (see next section), but also to search for K-isomers in that nucleus.

To detect events from the decay of possible isomeric states, correlations of the type ER (implantation signal)–CE (possibly in prompt coincidence with a γ event)–α decay / SF (from [255]Rf or [251]No) were searched for. But still one had to consider a possible population of the known $5/2^+$ isomeric state in [255]Rf ($E^* \approx 135$ keV, $T_{1/2} = 50 \pm 17$ μs) [140]. This isomer is known to decay essentially by CE emission of $E < 150$ keV. So, being conservative, CE energies above 200 keV could be assigned to the decay of another isomeric state. Two activities were identified [80]: (a) one with a half-life of $T_{1/2} = 38^{+12}_{-7}$ μs and CE energies essentially below 370 keV, and (b) one with a half-life of $T_{1/2} = 15^{+6}_{-4}$ μs and CE energies above 370 keV. Based on the observation of three correlations of the type ER–CE1–CE2–α/SF the events with the longer half-life were attributed to an isomeric state at $E^* \approx (1.15–1.45)$ MeV, the one with the lower half-life to a state at $E^* \approx (0.9–1.2)$ MeV.

For some of the CE also γ events were observed in prompt coincidence, but no line structure was visible due to low statistics. Also no spin and parity values could be determined. This has to be left for further, more detailed studies.

2.5.5 Spontaneous fission properties of [255,256,258]Rf

Important features in spontaneous fission studies are the determination of the total energy release (<TKE>) and the mass distribution of the fission fragments. Implantation of nuclei into silicon detectors is, however, not a well-suited technique for such investigations: (a) due to the high ionization density of the heavy fission fragments, part of the created charge carriers will recombine and so there is no linear dependence between the height of the signal and the energy of the fission fragments; (b) the implantation depth of the ER (typically <10 μm) is lower than the range of the fission products (typically 20–25 μm). Therefore, recorded signals will be a mixture of the sum of the energy of both fragments (E(SF1)+E(SF2)) and the energy of one fragment and the energy loss of the other one (E(SF1)+ΔE(SF2) or ΔE(SF1)+E(SF2)). Despite of these restrictions the [50]Ti beam was used to obtain more precise information on (<TKE>) of [255,256]Rf. Quite precise measurements of (<TKE>) and the

mass distribution have been reported for ^{258}Rf [163]. As the experimental conditions (detector system, calibration, implantation depth) were quite similar for ^{255}Rf (production: ^{207}Pb(^{50}Ti,2n)^{255}Rf), ^{256}Rf (production: ^{208}Pb(^{50}Ti,2n)^{256}Rf), and ^{258}Rf (production: ^{209}Bi(^{50}Ti,1n)^{258}Db $\xrightarrow{EC}$ ^{258}Rf), the measurement of ^{258}Rf was used as a reference for improving the data for ^{255,256}Rf. In addition, results from a previous SF study of ^{252}No [85] were reanalyzed for comparison. Using (only) the events recorded as coincidences in the 'stop' and 'box' detectors (see Sect. 2.5.1) we obtained [80] (Previously reported values are given in brackets):

$$< \text{TKE} > (^{255}\text{Rf}) = 201.2 \pm 0.9\,\text{MeV}(199 \pm 3\,\text{MeV}\,[139])$$
$$< \text{TKE} > (^{256}\text{Rf}) = 197.5 \pm 1.0\text{MeV}(198.9 \pm 4.4\,\text{MeV}\,[162]) \qquad (6)$$
$$< \text{TKE} > (^{258}\text{Rf}) = 197.9 \pm 0.7\,\text{MeV}(197.6 \pm 1.1\,\text{MeV}\,[162])$$

The <TKE> distributions were found to be narrower than for ^{252}No, which is known to fission asymmetrically [164]. This is seen as a signature for (nearly) symmetric fission of the three investigated Rf isotopes, in accordance with the conclusions drawn for ^{256,258}Rf in [163].

The new results (red squares) are compared with published <TKE> values in Fig. 16; the lines refer to empirical systematics from Unik et al. [166] (dashed line) and Viola et al. [167] (full lines). In addition, the <TKE> distributions were analyzed with respect to possible contributions for 'bimodal' fission. Small effects for ^{255,256}Rf were indicated, but far from being unambiguous. Therefore such studies have to be left for further investigations using experimental techniques more suited for such cases.

2.5.6 Decay study of isotopes produced in the reaction ^{181}Ta(^{48}Ca,*xpyn*)$^{229-xpyn}$Np

Nuclei in the vicinity of closed proton and neutron shells are of specific interest, as their decay properties reflect changes in the strength of the shells along isotone or isotope lines. From the results of a recent decay study of the uranium isotopes ^{222}U and ^{221}U that were identified for the first time, a weakening of the influence of the $N = 126$ shell on the decay properties of these uranium isotopes was concluded [168].

Thus, the investigation of the $N = 126$ shell strength towards elements with higher Z numbers is of interest. As a first step in this direction and also to test the performance of the new SHIP detector system COMPASS (see Sect. 2.5.1), we performed an investigation of nuclei produced in bombardments of ^{181}Ta with ^{48}Ca, specifically those starting from ^{225}Np (4n-channel), ^{226}Np (3n-channel), ^{222}Pa (α3n-channel), ^{225}U (p2n-channel), and ^{223}Pa (α2n) [20]. We also had the intension to obtain decay data of higher quality for ^{225,226}Np and possibly to identify the then unknown isotope ^{224}Np that has meanwhile been observed [169]. From a technical point of view, it was of interest that the α-decay chains of ^{225,226}Np include very short-lived members, ^{218}Ac ($T_{1/2} = 1.08\,\mu\text{s}$) in the case of ^{226}Np, ^{221}Pa ($T_{1/2} = 5.9\,\mu\text{s}$), and ^{217}Ac ($T_{1/2} = 69\,\text{ns}$) in the case of ^{225}Np, which appear as pile-up events in previous experiments using the implantation technique and analogue electronics, but were now measured with the fully-digitized detector system COMPASS.
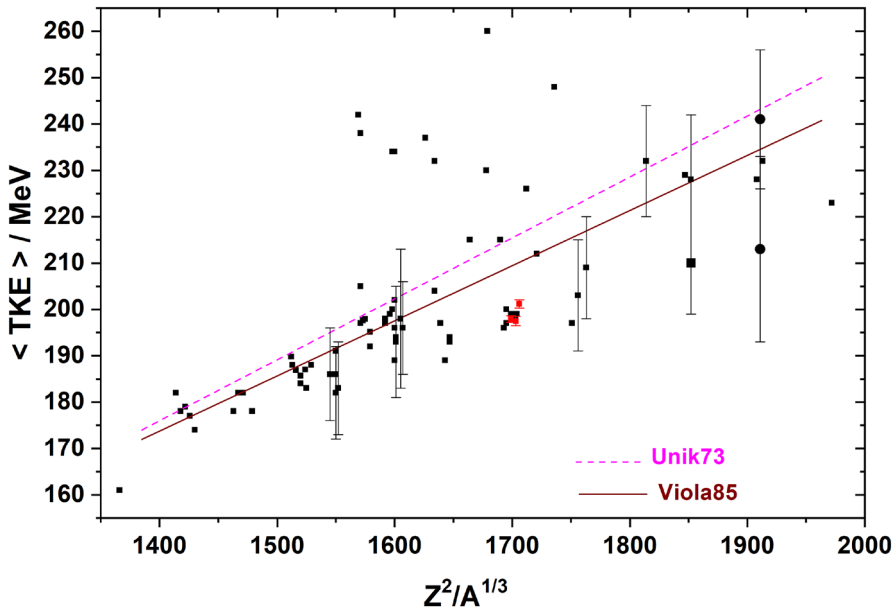
Fig. 16 Systematics of total energy release in spontaneous fission. Reprinted by permission from Nature/Springer, Eur. Phys. J. A, Spontaneous fission properties of superheavy elements, Heßberger [165]

In general, published decay data were reproduced or improved. New decay data were obtained for ^{225}Np, ^{226}Np, and ^{222}Pa. For ^{226}Np and ^{222}Pa new high-energy α transitions of 8.18 ± 0.02 MeV (^{226}Np) and 8.63 ± 0.04 MeV (^{222}Pa) were observed that had not been reported before. For ^{225}Np α-decay energy and half-life were measured simultaneously for the first time. Andreev et al. [170] had reported only an energy of 8.63 MeV, while Devaraja et al. [171] gave a half-life value of ≈ 3.8 ms obtained from the time difference between the decays of ^{229}Am and ^{225}Np of 5.5 ms of one observed event, but they did not report an energy value, as the event was observed as a pile-up with the daughter nucleus ^{221}Ac. The SHIP experiment of Mistry et al. [20] delivered a somewhat higher α-decay energy of 8.8 ± 0.1 MeV and on the basis of two observed events a half-life of $0.31^{+0.75}_{-0.13}$ ms, which is about an order of magnitude lower than the value given by Devaraja et al..

3 Summary and conclusions

In recent years, the experiments at SHIP focussed on detailed investigations of the nuclear structure of nuclei in the region $Z = 102$–105 in the vicinity of the deformed neutron shell closure at $N = 152$. Nuclides in this region can still be produced with rates that result in rather high statistics even in shorter experiments. We have performed systematic studies of different and often complementary nuclear properties by $\alpha-\gamma$ spectroscopy, by direct mass measurements, and by laser spectroscopy contributing to a better understanding of the nuclear structure evolution in this region. In particu-

lar, we have studied the evolution of the shell closure at $N = 152$ in the elements $Z = 102–105$ investigating binding energies of $^{252-255}$No and ^{255,256}Lr isotopes from directly measured nuclear masses [66, 67], by the change in nuclear charge radii for $^{252-255}$No by laser spectroscopy [110], and by the determination of excited nuclear states in ^{255,257,258}Rf and ^{257,258}Db isotopes by α–γ spectroscopy. We obtained more detailed information on the structure and the decay modes of these neutron-deficient Rf and Db isotopes. In particular, we identified the electron-capture-decay of ^{258}Db unambiguously by delayed coincidences with X-rays in the daughter. This approach will become more important in the future as EC decays play an increasingly important role in the assignment of decay chains originating from more neutron-rich superheavy nuclides. Also, the complex decay scheme of ^{258}Db was further elucidated and evidence for two long-lived isomeric states in ^{258}Db was revealed [81].

Accurate mass measurements of several No and Lr isotopes provided anchor points in the mass surface that allowed us to improve the masses of heavier nuclides that are linked by α-decay chains, for example ^{270}Ds [77]. The determination of ground-state masses of odd–odd and odd-A nuclides by mass spectrometry provide Q-values essential to establish unambiguous nuclear level schemes in conjunction with decay spectroscopy. In the future, the identification of isomeric states and the accurate determination of their excitation energy by mass spectrometry with SHIPTRAP will be exploited. Thanks to the powerful PI-ICR technique this is now possible for long-lived isomers with lowest excitation energies of tens of keV. Additional synergies are expected from trap-assisted decay spectroscopy experiments for select nuclides where SHIPTRAP will be used as high-resolution mass separator to provide not only isotopically pure samples, but even nuclear-state selected samples for subsequent decay studies. The capabilities of this approach have already been demonstrated for ^{213}Ra [172].

Information on the deformation and shape of heavy nuclei can be obtained from the observation of rotational bands and from hyperfine laser spectroscopy and optical isotope shift measurements. Laser spectroscopy also provides information on nuclear spins, electromagnetic nuclear moments and changes in the mean-square charge radii [92]. Together with decay spectroscopy this gives a handle on nuclear configurations. Laser spectroscopy of nobelium isotopes has demonstrated that this method can be applied to the heaviest elements even if no experimental data on the atomic structure exists. From the first experiments information on the changes in the mean-square charge radii and the deformation in three No isotopes were achieved [110]. The results are in good agreement with theoretical calculations by energy-density functionals. The hyperfine spectroscopy of ^{253}No provided the nuclear dipole and quadrupole moments and confirmed the spin-parity assignment from earlier decay spectroscopy experiments.

The combination of three complementary approaches, decay spectroscopy, laser spectroscopy, and mass spectrometry, for very heavy nuclides is presently only available at SHIP at the GSI. One prominent example where this may help us to solve a long-standing puzzle is the structure of the $8^- K$ isomer in ^{254}No. This isomer has been investigated by decay spectroscopy several years ago but its structure is still debated [129, 137, 159, 173]. Two quasi-particle configurations in ^{254}No can form an 8^- state, a quasi-neutron and one quasi-proton configuration. Despite several experi-

mental attempts it has not been possible to unambiguously determine the configuration of this isomer yet. The answer could be revealed by high-resolution laser spectroscopy by a measurement of the magnetic moment. Such an experiment will be enabled in the near future by the new gas-jet setup discussed in Sect. 2.4.5.

The extension of our experiments to heavier nuclides will be accompanied by continuous developments of new methods and improved experimental setups. The PI-ICR method, the COMPASS detector and the gas-jet setup are examples of this successful strategy. Our experimental program will also benefit from future upgrades of the linear accelerator chain at the GSI [174] that are expected to result in an increase of primary-beam intensities by up to an order of magnitude. The use of hot-fusion reactions with radioactive actinide targets will be needed to extend the reach towards more neutron-rich nuclei. While the known-how in handling radioactive actinide targets exists at GSI as shown in several experiments as SHIP [86] and TASCA [175, 177], some challenges remain. One limiting factor is the reduced transmission of SHIP for more asymmetric fusion reactions, which can only be overcome in a future upgrade.

In addition to the exploration of the region of the heaviest elements, the study of selected neutron-deficient isotopes of lighter nuclides is an area where experiments at SHIP remain competitive. The region around the Np isotopes studied in the COMPASS commissioning is one example. The search for exotic decay modes such as beta-delayed fission [176] is another topic of interest.

Declarations

Conflict of interest The authors have no relevant financial or non-financial interests to disclose.

References

1. A. Sobiczewski, F. Gareev, B. Kalinkin, Phys. Lett. **22**(4), 500 (1966). https://doi.org/10.1016/0031-9163(66)91243-1

2. H. Meldner, Ark. Fys. **36**, 593–8 (1967) https://escholarship.org/uc/item/28q2j00w
3. M.G. Mayer, Phys. Rev. **74**, 235 (1948). https://doi.org/10.1103/PhysRev.74.235
4. O. Haxel, J.H.D. Jensen, H.E. Suess, Phys. Rev. **75**, 1766 (1949). https://doi.org/10.1103/PhysRev.75.1766.2
5. S.G. Nilsson, C.F. Tsang, A. Sobiczewski, Z. Szymański, S. Wycech, C. Gustafson, I.L. Lamm, P. Möller, B. Nilsson, Nucl. Phys. A **131**(1), 1 (1969). https://doi.org/10.1016/0375-9474(69)90809-4
6. S. Hofmann, G. Münzenberg, Rev. Mod. Phys. **72**(3), 733 (2000). https://doi.org/10.1103/RevModPhys.72.733
7. K. Morita, K. Morimoto, D. Kaji, H. Haba, K. Ozeki, Y. Kudou, T. Sumita, Y. Wakabayashi, A. Yoneda, K. Tanaka et al., J. Phys. Soc. Jpn. **81**(10), 103201 (2012). https://doi.org/10.1143/JPSJ.81.103201
8. Y.T. Oganessian, V.K. Utyonkov, Nucl. Phys. A **944**, 62 (2015). https://doi.org/10.1016/j.nuclphysa.2015.07.003
9. A. Baran, M. Kowal, P.G. Reinhard, L. Robledo, A. Staszczak, M. Warda, Nucl. Phys. A **944**, 442 (2015). https://doi.org/10.1016/j.nuclphysa.2015.06.002
10. S. Giuliani, Z. Matheson, W. Nazarewicz et al., Rev. Mod. Phys. **91**, 011001 (2019). https://doi.org/10.1103/RevModPhys.91.011001
11. C.F. v. Weizsäker, Z. Phys. **96**(7–8), 431 (1935). https://doi.org/10.1007/bf01337700
12. V. Strutinsky, Nucl. Phys. A **95**(2), 420 (1967). https://doi.org/10.1016/0375-9474(67)90510-6
13. A. Sobiczewski, Acta Phys. Polon. B **46**(3), 551 (2015). https://doi.org/10.5506/APhysPolB.46.551
14. K. Rutz, M. Bender, T. Bürvenich, T. Schilling, P.G. Reinhard, J.A. Maruhn, W. Greiner, Phys. Rev. C **56**(1), 238 (1997). https://doi.org/10.1103/PhysRevC.56.238
15. M. Bender, P.H. Heenen, P.G. Reinhard, Rev. Mod. Phys. **75**(1), 121 (2003). https://doi.org/10.1103/RevModPhys.75.121
16. M. Bender, W. Nazarewicz, P.G. Reinhard, Phys. Lett. B **515**(1), 42 (2001). https://doi.org/10.1016/S0370-2693(01)00863-2
17. G. Münzenberg, W. Faust, S. Hofmann, P. Armbruster, K. Güttner, H. Ewald, Nucl. Instrum. Meth. **161**(1), 65 (1979). https://doi.org/10.1016/0029-554X(79)90362-8
18. G. Münzenberg, K. Morita, Nucl. Phys. A **944**, 3 (2015). https://doi.org/10.1016/j.nuclphysa.2015.06.007
19. D. Ackermann, A. Mistry, F. Heßberger, B. Andel, S. Antalic, M. Block, L. Caceres, P. Chhetri, F. Dechery, C. Droese, C. Düllmann, F. Giacoppo, J. Hoffmann, O. Kaleja, O. Kamalou, N. Kurz, J. Khuyagbaatar, R. Mändl, T. Murböck, M. Laatiaoui, J. Maurer, J. Piot, S. Raeder, H. Savajols, O. Sorlin, C. Stodel, J. Thomas, M. Vostinar, P. Wieczorek, A. Yakushev, Z. Zhang, Nucl. Instrum. Methods Phys. Res. Sect. A **907**, 81 (2018). https://doi.org/10.1016/j.nima.2018.01.096
20. A. Mistry, J. Khuyagbaatar, F. Heßberger, D. Ackermann, B. Andel, S. Antalic, M. Block, P. Chhetri, F. Dechery, C. Droese, C. Düllmann, F. Giacoppo, J. Hoffmann, O. Kaleja, N. Kurz, M. Laatiaoui, L. Lens, J. Maurer, P. Mosat, J. Piot, S. Raeder, M. Vostinar, A. Yakushev, Z. Zhang, Nucl. Phys. A **987**, 337 (2019). https://doi.org/10.1016/j.nuclphysa.2019.05.003
21. M. Block, Nucl. Phys. A **944**, 471 (2015). https://doi.org/10.1016/j.nuclphysa.2015.09.009
22. H. Backe, W. Lauth, M. Block, M. Laatiaoui, Nucl. Phys. A **944**, 492 (2015). https://doi.org/10.1016/j.nuclphysa.2015.07.002
23. F. Lautenschläger, P. Chhetri, D. Ackermann, H. Backe, M. Block, B. Cheal, A. Clark, C. Droese, R. Ferrer, F. Giacoppo, S. Götz, F. Heßberger, O. Kaleja, J. Khuyagbaatar, P. Kunz, A. Mistry, M. Laatiaoui, W. Lauth, S. Raeder, T. Walther, C. Wraith, Nucl. Instrum. Methods Phys. Res. Sect. B **383**, 115 (2016). https://doi.org/10.1016/j.nimb.2016.06.001
24. G. Münzenberg, P. Armbruster, G. Berthes, F. Hessberger, S. Hofmann, W. Reisdorf, K.H. Schmidt, H.J. Schött, Nucl. Instrum. Methods Phys. Res., Sect. B **26**(1–3), 294 (1987). https://doi.org/10.1016/0168-583x(87)90766-x
25. G. Münzenberg, P. Armbruster, W. Faust, S. Hofmann, W. W. Reisdorf, K.H. Schmidt, K. Valli, H. Ewald, K. Güttner, H.G. Clerc, W. Lang, GSI Jahresbericht 1977 **GS-J-1-78, 75** (1978)
26. Y.T. Oganessian, *Classical and Quantum Mechanical Aspects of Heavy Ion Collisions*, Lecture Notes in Physics, vol. 33. (Springer, Berlin, 1975), pp. 221–252. https://doi.org/10.1007/3-540-07025-7_13
27. F.P. Heßberger, G. Münzenberg, P. Armbruster, G. Berthes, W. Faust, S. Hofmann, W. Reisdorf, K.H. Schmidt, H. Ewald, K. Güttner, *Heavy Ion Interactions Around the Coulomb Barrier*, Lecture Notes in Physics, vol. 317. (Springer, Berlin, 1988). https://doi.org/10.1007/3-540-50578-4_35
28. S. Hofmann, Rep. Prog. Phys. **61**(6), 639 (1998). https://doi.org/10.1088/0034-4885/61/6/002

29. D. Marx, F. Nickel, G. Münzenberg, K. Güttner, H. Ewald, W. Faust, S. Hofmann, H. Schött, W. Thalheimer, Nucl. Instrum. Methods **163**(1), 15 (1979). https://doi.org/10.1016/0029-554x(79)90028-4

30. H. Folger, W. Hartmann, F. Heßberger, S. Hofmann, J. Klemm, G. Münzenberg, V. Ninov, W. Thalheimer, P. Armbruster, Nucl. Instrum. Methods Phys. Res. Sect. A **362**(1), 64 (1995). https://doi.org/10.1016/0168-9002(95)00527-7

31. B. Kindler, D. Ackermann, W. Hartmann, F.P. Heßberger, S. Hofmann, B. Lommel, R. Mann, J. Steiner, Nucl. Instrum. Methods Phys. Res. Sect. A **561**(1), 107 (2006). https://doi.org/10.1016/j.nima.2005.12.232

32. R. Mann, D. Ackermann, S. Antalic, H.G. Burkhard, P. Cagarda, G. Gemalies-Datz, W. Hartmann, F. Heßberger, S. Hofmann, B. Kindler, P. Kuusiniemi, B. Lommel, S. Sarov, H. Schött, J. Steiner, GSI Scientific Report 2003 GSI 2004-1, 224 (2004)

33. H. Gäggeler, D. Jost, A. Türler, P. Armbruster, W. Brüchle, H. Folger, F. Heßberger, S. Hofmann, G. Münzenberg, V. Ninov, W. Reisdorf, M. Schädel, K. Sümmerer, J. Kratz, U. Scherer, M. Leino, Nucl. Phys. A **502**, 561 (1989). https://doi.org/10.1016/0375-9474(89)90689-1

34. F.P. Heßberger, Eur. Phys. J. D **45**(1), 33–37 (2007). https://doi.org/10.1140/epjd/e2007-00146-1

35. W. Reisdorf, M. Schädel, Z. Phys. A **343**(1), 47 (1992). https://doi.org/10.1007/BF01291597

36. D. Lunney, J.M. Pearson, C. Thibault, Rev. Mod. Phys. **75**(3), 1021 (2003). https://doi.org/10.1103/RevModPhys.75.1021

37. M. Block, C. Bachelet, G. Bollen, M. Facina, C.M. Folden III., C. Guénaut, A.A. Kwiatkowski, D.J. Morrissey, G.K. Pang, A. Prinke et al., Nucl. Instrum. Meth. B **266**(19), 4521 (2008). https://doi.org/10.1016/j.nimb.2008.05.098

38. C. Rauth, D. Ackermann, G. Audi, M. Block, A. Chaudhuri, S. Eliseev, F. Herfurth, F. Hessberger, S. Hofmann, H.J. Kluge et al., Eur. Phys. J. Spec. Top. **150**(1), 329 (2007). https://doi.org/10.1140/epjst/e2007-00339-8

39. R. Orford, N. Vassh, J.A. Clark, G.C. McLaughlin, M.R. Mumpower, G. Savard, R. Surman, A. Aprahamian, F. Buchinger, M.T. Burkey, D.A. Gorelov, T.Y. Hirsh, J.W. Klimes, G.E. Morgan, A. Nystrom, K.S. Sharma, Phys. Rev. Lett. **120**(26), 262702 (2018). https://doi.org/10.1103/PhysRevLett.120.262702

40. M. Vilen, J. Kelly, A. Kankainen, M. Brodeur, A. Aprahamian, L. Canete, T. Eronen, A. Jokinen, T. Kuta, I. Moore, M. Mumpower, D. Nesterenko, H. Penttilä, I. Pohjalainen, W. Porter, S. Rinta-Antila, R. Surman, A. Voss, J. Äystö, Phys. Rev. Lett. (2018). https://doi.org/10.1103/physrevlett.120.262701

41. V. Manea, J. Karthein, D. Atanasov, M. Bender, K. Blaum, T. Cocolios, S. Eliseev, A. Herlert, J. Holt, W. Huang, Y. Litvinov, D. Lunney, J. Menéndez, M. Mougeot, D. Neidherr, L. Schweikhard, A. Schwenk, J. Simonis, A. Welker, F. Wienholtz, K. Zuber, Phys. Rev. Lett. (2020). https://doi.org/10.1103/physrevlett.124.092502

42. K. Blaum, Phys. Rep. **425**(1), 1 (2006). https://doi.org/10.1016/j.physrep.2005.10.011

43. H.J. Kluge, Int. J. Mass Spectrom. **349**, 26 (2013). https://doi.org/10.1016/j.ijms.2013.04.017

44. K. Blaum, J. Dilling, W. Nörtershäuser, Phys. Scr. **2013**(T152), 014017 (2013). https://doi.org/10.1088/0031-8949/2013/T152/014017

45. M. Block, Radiochim. Acta **107**(7), 603 (2019). https://doi.org/10.1515/ract-2019-0002

46. J. Dilling, D. Ackermann, J. Bernard, F.P. Hessberger, S. Hofmann, W. Hornung, H.J. Kluge, E. Lamour, M. Maier, R. Mann et al., Hyperfine Interact. **127**(1–4), 491 (2000). https://doi.org/10.1023/A:1012638322226

47. J.B. Neumayr, L. Beck, D. Habs, S. Heinz, J. Szerypo, P. Thirolf, V. Varentsov, F. Voit, D. Ackermann, D. Beck et al., Nucl. Instrum. Meth. B **244**(2), 489 (2006). https://doi.org/10.1016/j.nimb.2005.10.017

48. C. Droese, S. Eliseev, K. Blaum, M. Block, F. Herfurth, M. Laatiaoui, F. Lautenschläger, E.M. Ramirez, L. Schweikhard, V.V. Simon et al., Nucl. Instrum. and Meth. B **338**, 126 (2014). https://doi.org/10.1016/j.nimb.2014.08.004

49. O. Kaleja, B. Anđelić, K. Blaum, M. Block, P. Chhetri, C. Droese, C. Düllmann, M. Eibach, S. Eliseev, J. Even, S. Götz, F. Giacoppo, N. Kalantar-Nayestanaki, M. Laatiaoui, E.M. Ramirez, A. Mistry, T. Murböck, S. Raeder, L. Schweikhard, P. Thirolf, Nucl. Instrum. Methods Phys. Res. Sect. B **463**, 280 (2020). https://doi.org/10.1016/j.nimb.2019.05.009

50. F. Herfurth, Nucl. Instrum. Meth. B **204**, 587 (2003). https://doi.org/10.1016/S0168-583X(02)02135-3

51. P. Schury, M. Wada, Y. Ito, D. Kaji, H. Haba, Y. Hirayama, S. Kimura, H. Koura, M. MacCormick, H. Miyatake, J. Moon, K. Morimoto, K. Morita, I. Murray, A. Ozawa, M. Rosenbusch, M. Reponen,

A. Takamine, T. Tanaka, Y. Watanabe, H. Wollnik, Nucl. Instrum. Methods Phys. Res. Sect. B **407**, 160 (2017). https://doi.org/10.1016/j.nimb.2017.06.014

52. J. Ketelaer, J. Krämer, D. Beck, K. Blaum, M. Block, K. Eberhardt, G. Eitel, R. Ferrer, C. Geppert, S. George et al., Nucl. Instrum. Meth. A **594**(2), 162 (2008). https://doi.org/10.1016/j.nima.2008.06.023

53. T. Eronen, V.S. Kolhinen, V.V. Elomaa, D. Gorelov, U. Hager, J. Hakala, A. Jokinen, A. Kankainen, P. Karvonen, S. Kopecky et al., *Three Decades of Research Using IGISOL Technique at the University of Jyväskylä* (Springer, Berlin, 2014), pp. 61–81. https://doi.org/10.1007/978-94-007-5555-0

54. G. Savard, G. Bollen, H.J. Kluge, R. Moore, T. Otto, L. Schweikhard, H. Stolzenberg, U. Wiess et al., Phys. Lett. A **158**(5), 247 (1991). https://doi.org/10.1016/0375-9601(91)91008-2

55. S. Eliseev, K. Blaum, M. Block, C. Droese, M. Goncharov, E.M. Ramirez, D.A. Nesterenko, Y.N. Novikov, L. Schweikhard, Phys. Rev. Lett. **110**(8), 082501 (2013). https://doi.org/10.1103/PhysRevLett.110.082501

56. S. Eliseev, K. Blaum, M. Block, A. Dörr, C. Droese, T. Eronen, M. Goncharov, M. Höcker, J. Ketter, E.M. Ramirez et al., Appl. Phys. B **114**(1–2), 107 (2014). https://doi.org/10.1007/s00340-013-5621-0

57. M. König, G. Bollen, H.J. Kluge, T. Otto, J. Szerypo, Int. J. Mass Spectrom. Ion Process. **142**(1), 95 (1995). https://doi.org/10.1016/0168-1176(95)04146-C

58. S. Eliseev, K. Blaum, M. Block, S. Chenmarev, H. Dorrer, C.E. Düllmann, C. Enss, P. Filianin, L. Gastaldo, M. Goncharov et al., Phys. Rev. Lett. **115**(6), 062501 (2015). https://doi.org/10.1103/PhysRevLett.115.062501

59. A.A. Kwiatkowski et al., Hyperfine Interact. **225**(1–3), 143 (2013). https://doi.org/10.1007/978-94-007-7963-1_16

60. G. Bollen, R.B. Moore, G. Savard, H. Stolzenberg, J. Appl. Phys. **68**(9), 4355 (1990). https://doi.org/10.1063/1.346185

61. C. Droese, M. Block, M. Dworschak, S. Eliseev, E.M. Ramirez, D. Nesterenko, L. Schweikhard, Nucl. Instrum. Meth. A **632**(1), 157 (2011). https://doi.org/10.1016/j.nima.2010.12.176

62. S. Rahaman, M. Block, D. Ackermann, D. Beck, A. Chaudhuri, S. Eliseev, H. Geissel, D. Habs, F. Herfurth, F. Heßberger et al., Int. J. Mass Spectrom. **251**(2), 146 (2006). https://doi.org/10.1016/j.ijms.2006.01.049

63. A. Martın, D. Ackermann, G. Audi, K. Blaum, M. Block, A. Chaudhuri, Z. Di, S. Eliseev, R. Ferrer, D. Habs et al., Eur. Phys. J. A **34**(4), 341 (2007). https://doi.org/10.1140/epja/i2007-10520-5

64. C. Weber, V.V. Elomaa, R. Ferrer, C. Fröhlich, D. Ackermann, J. Äystö, G. Audi, L. Batist, K. Blaum, M. Block et al., Phys. Rev. C **78**(5), 054310 (2008). https://doi.org/10.1103/PhysRevC.78.054310

65. C. Rauth, D. Ackermann, K. Blaum, M. Block, A. Chaudhuri, Z. Di, S. Eliseev, R. Ferrer, D. Habs, F. Herfurth et al., Phys. Rev. Lett. **100**(1), 012501 (2008). https://doi.org/10.1103/PhysRevLett.100.012501

66. M. Block, D. Ackermann, K. Blaum, C. Droese, M. Dworschak, S. Eliseev, T. Fleckenstein, E. Haettner, F. Herfurth, F.P. Heßberger et al., Nature **463**(7282), 785 (2010). https://doi.org/10.1038/nature08774

67. E.M. Ramirez et al., Science **337**, 1207 (2012). https://doi.org/10.1126/science.1225636

68. F. Giacoppo et al., Acta Phys. Pol. B **48**(3), 423 (2017). https://doi.org/10.5506/APhysPolB.48.423

69. M. Eibach, T. Beyer, K. Blaum, M. Block, C.E. Düllmann, K. Eberhardt, J. Grund, S. Nagy, H. Nitsche, W. Nörtershäuser et al., Phys. Rev. C **89**(6), 064318 (2014). https://doi.org/10.1103/PhysRevC.89.064318

70. Y. Ito, P. Schury, M. Wada, F. Arai, H. Haba, Y. Hirayama, S. Ishizawa, D. Kaji, S. Kimura, H. Koura, M. MacCormick, H. Miyatake, J. Moon, K. Morimoto, K. Morita, M. Mukai, I. Murray, T. Niwase, K. Okada, A. Ozawa, M. Rosenbusch, A. Takamine, T. Tanaka, Y. Watanabe, H. Wollnik, S. Yamaki, Phys. Rev. Lett. (2018). https://doi.org/10.1103/PhysRevLett.120.152501

71. P. Schury, M. Wada, Y. Ito, S. Naimi, T. Sonoda, H. Mita, A. Takamine, K. Okada, H. Wollnik, S. Chon et al., Nucl. Instrum. Meth. B **317**, 537 (2013). https://doi.org/10.1016/j.nimb.2013.06.025

72. R. Wolf, D. Beck, K. Blaum, C. Böhm, C. Borgmann, M. Breitenfeldt, N. Chamel, S. Goriely, F. Herfurth, M. Kowalska et al., Phys. Rev. Lett. **110**(4), 041101 (2013). https://doi.org/10.1103/PhysRevLett.110.041101

73. W.R. Plaß, T. Dickel, S. Purushothaman, P. Dendooven, H. Geissel, J. Ebert, E. Haettner, C. Jesch, M. Ranjan, M. Reiter et al., Nucl. Instrum. Meth. B **317**, 457 (2013). https://doi.org/10.1016/j.nimb.2013.07.063

74. C. Hornung, D. Amanbayev, I. Dedes, G. Kripko-Koncz, I. Miskun, N. Shimizu, S.A.S. Andrés, J. Bergmann, T. Dickel, J. Dudek, J. Ebert, H. Geissel, M. Górska, H. Grawe, F. Greiner, E. Haettner, T. Otsuka, W.R. Plaß, S. Purushothaman, A.K. Rink, C. Scheidenberger, H. Weick, S. Bagchi, A. Blazhev, O. Charviakova, D. Curien, A. Finlay, S. Kaur, W. Lippert, J.H. Otto, Z. Patyk, S. Pietri, Y.K. Tanaka, Y. Tsunoda, J.S. Winfield, Phys. Lett. B **802**, 135200 (2020). https://doi.org/10.1016/j.physletb.2020.135200

75. P. Schury, T. Niwase, M. Wada, P. Brionnet, S. Chen, T. Hashimoto, H. Haba, Y. Hirayama, D.S. Hou, S. Iimura, H. Ishiyama, S. Ishizawa, Y. Ito, D. Kaji, S. Kimura, H. Koura, J.J. Liu, H. Miyatake, J.Y. Moon, K. Morimoto, K. Morita, D. Nagae, M. Rosenbusch, A. Takamine, Y.X. Watanabe, H. Wollnik, W. Xian, S.X. Yan, Phys. Rev. C **104**, L021304 (2021). https://doi.org/10.1103/PhysRevC.104.L021304

76. M. Wang, W. Huang, F. Kondev, G. Audi, S. Naimi, Chin. Phys. C **45**(3), 030003 (2021). https://doi.org/10.1088/1674-1137/abddaf

77. M. Dworschak, M. Block, D. Ackermann, G. Audi, K. Blaum, C. Droese, S. Eliseev, T. Fleckenstein, E. Haettner, F. Herfurth et al., Phys. Rev. C **81**(6), 064312 (2010). https://doi.org/10.1103/PhysRevC.81.064312

78. A. Sobiczewski, K. Pomorski, Prog. Part. Nucl. Phys. **58**(1), 292 (2007). https://doi.org/10.1016/j.ppnp.2006.05.001

79. M.R. Bhat, Nuclear Data for Science and Technology. Springer, Berlin, pp. 817–821 (1992). https://doi.org/10.1007/978-3-642-58113-7_227. Data extracted using the NNDC On-Line Data Service from the ENSDF database, file revised as of (23.12.2020)

80. P. Mosat, F.P. Heßberger, S. Antalic, D. Ackermann, B. Andel, M. Block, S. Hofmann, Z. Kalaninova, B. Kindler, M. Laatiaoui, B. Lommel, A.K. Mistry, J. Piot, M. Vostinar, Phys. Rev. C (2020). https://doi.org/10.1103/physrevc.101.034310

81. M. Vostinar, F.P. Heßberger, D. Ackermann, B. Andel, S. Antalic, M. Block, C. Droese, J. Even, S. Heinz, Z. Kalaninova, I. Kojouharov, M. Laatiaoui, A.K. Mistry, J. Piot, H. Savajols, Eur. Phys. J. A (2019). https://doi.org/10.1140/epja/i2019-12701-y

82. F.P. Heßberger, S. Hofmann, B. Streicher, B. Sulignano, S. Antalic, D. Ackermann, S. Heinz, B. Kindler, I. Kojouharov, P. Kuusiniemi, M. Leino, B. Lommel, R. Mann, A.G. Popeko, Š Šáro, J. Uusitalo, A.V. Yeremin, Eur. Phys. J. A **41**(2), 145 (2009). https://doi.org/10.1140/epja/i2009-10826-2

83. B. Streicher, F.P. Heßberger, S. Antalic, S. Hofmann, D. Ackermann, S. Heinz, B. Kindler, J. Khuyagbaatar, I. Kojouharov, P. Kuusiniemi et al., Eur. Phys. J. A **45**(3), 275 (2010). https://doi.org/10.1140/epja/i2010-11005-2

84. J. Dvorak, W. Brüchle, M. Chelnokov, R. Dressler, C.E. Düllmann, K. Eberhardt, V. Gorshkov, E. Jäger, R. Krücken, A. Kuznetsov, Phys. Rev. Lett. **97**(24), 242501 (2006). https://doi.org/10.1103/PhysRevLett.97.242501

85. S. Hofmann, D. Ackermann, S. Antalic, H.G. Burkhard, V.F. Comas, R. Dressler, Z. Gan, S. Heinz, J.A. Heredia, F.P. Heßberger, Eur. Phys. J. A **32**(3), 251 (2007). https://doi.org/10.1140/epja/i2007-10373-x

86. S. Hofmann, S. Heinz, R. Mann, J. Maurer, J. Khuyagbaatar, D. Ackermann, S. Antalic, W. Barth, M. Block, H. Burkhard et al., Eur. Phys. J. A **48**(5), 62 (2012). https://doi.org/10.1140/epja/i2012-12062-1

87. B. Cheal, K. Flanagan, J. Phys. G Nucl. Part. Phys. **37**, 113101 (2010). https://doi.org/10.1088/0954-3899/37/11/113101

88. P. Campbell, I.D. Moore, M.R. Pearson, Prog. Part. Nucl. Phys. **86**, 127 (2016). https://doi.org/10.1016/j.ppnp.2015.09.003

89. H. Backe, M. Hies, H. Kunz, W. Lauth, O. Curtze, P. Schwamb, M. Sewtz, W. Theobald, R. Zahn, K. Eberhardt et al., Phys. Rev. Lett. **80**(5), 920 (1998). https://doi.org/10.1103/PhysRevLett.80.920

90. V. Letokhov, *Laser Photoionization Spectroscopy* (Academic Press INC, Orlando, 1987)

91. G.S. Hurst, M.G. Payne, Principles and Applications of Resonance Ionisation Spectroscopy (A. Hilger, 1988)

92. M. Block, M. Laatiaoui, S. Raeder, Prog. Part. Nucl. Phys. **116**, 103834 (2021). https://doi.org/10.1016/j.ppnp.2020.103834

93. J.B. Roberto, C.W. Alexander, R.A. Boll, J.D. Burns, J.G. Ezold, L.K. Felker, S.L. Hogle, K.P. Rykaczewski, Nucl. Phys. A **944**, 99 (2015). https://doi.org/10.1016/j.nuclphysa.2015.06.009

94. M. Sewtz, H. Backe, A. Dretzke, G. Kube, W. Lauth, P. Schwamb, K. Eberhardt, C. Grüning, P. Thörle, N. Trautmann, P. Kunz, J. Lassen, G. Passler, C.Z. Dong, S. Fritzsche, R.G. Haire, Phys. Rev. Lett **90**, 163002 (2003). https://doi.org/10.1103/PhysRevLett.90.163002
95. J. Blaise, J.F. Wyart, Tables Select. Constants **20**(8), 412 (1992)
96. M. Laatiaoui, W. Lauth, H. Backe, M. Block, D. Ackermann, B. Cheal, P. Chhetri, C.E. Düllmann, P. Van Duppen, J. Even et al., Nature **538**(7626), 495 (2016). https://doi.org/10.1038/nature19345
97. E. Eliav, A. Borschevsky, U. Kaldor, Nucl. Phys. News **29**(1), 16 (2019). https://doi.org/10.1080/10619127.2019.1571794
98. H. Backe, P. Kunz, W. Lauth, A. Dretzke, R. Horn, T. Kolb, M. Laatiaoui, M. Sewtz, D. Ackermann, M. Block et al., Eur. Phys. J. D **45**(1), 99 (2007). https://doi.org/10.1140/epjd/e2007-00198-1
99. M. Laatiaoui, H. Backe, M. Block, F.P. Heßberger, P. Kunz, F. Lautenschläger, W. Lauth, M. Sewtz, T. Walther, Eur. Phys. J. D **68**, 71 (2014). https://doi.org/10.1140/epjd/e2014-40617-6
100. M. Laatiaoui, H. Backe, M. Block, P. Chhetri, F. Lautenschläger, W. Lauth, T. Walther, Hyperfine Interact. **227**(1–3), 69 (2014). https://doi.org/10.1007/s10751-013-0971-x
101. S. Fritzsche, Eur. Phys. J. D **33**(1), 15 (2005). https://doi.org/10.1140/epjd/e2005-00013-1
102. A. Borschevsky, E. Eliav, M.J. Vilkas, Y. Ishikawa, U. Kaldor, Phys. Rev. A **75**(4), 042514 (2007). https://doi.org/10.1103/PhysRevA.75.042514
103. Y. Liu, R. Hutton, Y. Zou, Phys. Rev. A (2007). https://doi.org/10.1103/physreva.76.062503
104. P. Indelicato et al., Eur. Phys. J. D **45**, 155 (2007). https://doi.org/10.1140/epjd/e2007-00229-y
105. V.A. Dzuba, M.S. Safronova, U.I. Safronova, Phys. Rev. A **90**(1), 012504 (2014). https://doi.org/10.1103/PhysRevA.90.012504
106. P. Chhetri, D. Ackermann, H. Backe, M. Block, B. Cheal, C.E. Düllmann, J. Even, R. Ferrer, F. Giacoppo, S. Götz, F.P. Heßberger, O. Kaleja, J. Khuyagbaatar, P. Kunz, M. Laatiaoui, F. Lautenschläger, W. Lauth, E.M. Ramirez, A.K. Mistry, S. Raeder, C. Wraith, T. Walther, A. Yakushev, Europ. Phys. J. D **71**(7), 195 (2017). https://doi.org/10.1140/epjd/e2017-80122-x
107. P. Chhetri, C. Moodley, S. Raeder, M. Block, F. Giacoppo, S. Götz, F. Heßberger, M. Eibach, O. Kaleja, M. Laatiaoui, A. Mistry, T. Murböck, T. Walther, Acta Phys. Pol. B **49**(3), 599 (2018). https://doi.org/10.5506/APhysPolB.49.599
108. P. Chhetri, D. Ackermann, H. Backe, M. Block, B. Cheal, C. Droese, C.E. Düllmann, J. Even, R. Ferrer, F. Giacoppo, S. Götz, F. Heßberger, M. Huyse, O. Kaleja, J. Khuyagbaatar, P. Kunz, M. Laatiaoui, F. Lautenschläger, W. Lauth, N. Lecesne, L. Lens, E.M. Ramirez, A. Mistry, S. Raeder, P.V. Duppen, T. Walther, A. Yakushev, Z. Zhang, Phys. Rev. Lett. **120**, 263003 (2018). https://doi.org/10.1103/PhysRevLett.120.263003
109. T.K. Sato, M. Asai, A. Borschevsky, R. Beerwerth, Y. Kaneya, H. Makii, A. Mitsukai, Y. Nagame, A. Osa, A. Toyoshima et al., J. Am. Chem. Soc. **140**(44), 14609 (2018). https://doi.org/10.1021/jacs.8b09068
110. S. Raeder, D. Ackermann, H. Backe, R. Beerwerth, J. Berengut, M. Block, A. Borschevsky, B. Cheal, P. Chhetri, C.E. Düllmann, V. Dzuba, E. Eliav, J. Even, R. Ferrer, V. Flambaum, S. Fritzsche, F. Giacoppo, S. Götz, F. Heßberger, M. Huyse, U. Kaldor, O. Kaleja, J. Khuyagbaatar, P. Kunz, M. Laatiaoui, F. Lautenschläger, W. Lauth, A. Mistry, E.M. Ramirez, W. Nazarewicz, S. Porsev, M. Safronova, U. Safronova, B. Schuetrumpf, P.V. Duppen, T. Walther, C. Wraith, A. Yakushev, Phys. Rev. Lett. (2018). https://doi.org/10.1103/PhysRevLett.120.232503
111. Y.T. Oganessian, V.K. Utyonkov, Y.V. Lobanov, F.S. Abdullin, A.N. Polyakov, I.V. Shirokovsky, Y.S. Tsyganov, A.N. Mezentsev, S. Iliev, V.G. Subbotin, A.M. Sukhov, K. Subotic, O.V. Ivanov, A.N. Voinov, V.I. Zagrebaev, K.J. Moody, J.F. Wild, N.J. Stoyer, M.A. Stoyer, R.W. Lougheed, Phys. Rev. C (2001). https://doi.org/10.1103/physrevc.64.054606
112. S. Antalic, F.P. Heßberger, S. Hofmann, D. Ackermann, S. Heinz, B. Kindler, I. Kojouharov, P. Kuusiniemi, M. Leino, B. Lommel et al., Eur. Phys. J. A **38**(2), 219 (2008). https://doi.org/10.1140/epja/i2008-10665-7
113. F.P. Heßberger, S. Hofmann, D. Ackermann, S. Antalic, B. Kindler, I. Kojouharov, P. Kuusiniemi, M. Leino, B. Lommel, R. Mann, K. Nishio, A.G. Popeko, B. Sulignano, S. Saro, B. Streicher, M. Venhart, A.V. Yeremin, Eur. Phys. J. A **30**(3), 561 (2006). https://doi.org/10.1140/epja/i2006-10137-2
114. H. Backe, A. Dretzke, R.G. Haire, P. Kunz, W. Lauth, M. Sewtz, N. Trautmann et al., Hyperfine Interact **162**(1–4), 3 (2005)
115. Y. Zou, C.F. Fischer, Phys. Rev. Lett. **88**(18), 183001 (2002). https://doi.org/10.1103/PhysRevLett.88.183001

116. S. Fritzsche, C.Z. Dong, F. Koike, A. Uvarov, Eur. Phys. J. D **45**(1), 107 (2007). https://doi.org/10.1140/epjd/e2007-00136-3

117. A. Borschevsky, E. Eliav, M.J. Vilkas, Y. Ishikawa, U. Kaldor, Eur. Phys. J. D **45**(1), 115 (2007). https://doi.org/10.1140/epjd/e2007-00130-9

118. E.V. Kahl, S. Raeder, E. Eliav, A. Borschevsky, J.C. Berengut, Phys. Rev. A **104**, 052810 (2021). https://doi.org/10.1103/PhysRevA.104.052810

119. T. Sato, M. Asai, A. Borschevsky, T. Stora, N. Sato, Y. Kaneya, K. Tsukada, C.E. Düllmann, K. Eberhardt, E. Eliav et al., Nature **520**(7546), 209 (2015). https://doi.org/10.1038/nature14342

120. T. Murböck, S. Raeder, P. Chhetri, K. Diaz, M. Laatiaoui, F. Giacoppo, M. Block, Hyperfine Interact. **241**, 35 (2020). https://doi.org/10.1007/s10751-019-1689-1

121. Y. Kudryavtsev, R. Ferrer, M. Huyse, P. Van den Bergh, P. Van Duppen, Nucl. Instrum. Methods Phys. Res. Sect. B **297**, 7 (2013). https://doi.org/10.1016/j.nimb.2012.12.008

122. S. Raeder, R. Ferrer, C. Granados, M. Huyse, T. Kron, Y. Kudryavtsev, N. Lecesne, J. Piot, J. Romans, H. Savajols, P.V. Duppen, K. Wendt, Nucl. Instrum. Methods Phys. Res. Sect. B (2020). https://doi.org/10.1016/j.nimb.2019.11.024

123. R. Ferrer et al., Nat. Commun. **8**, 14520 (2017). https://doi.org/10.1038/ncomms14520

124. A. Zadvornaya, P. Creemers, K. Dockx, R. Ferrer, L. Gaffney, W. Gins, C. Granados, M. Huyse, Y. Kudryavtsev, M. Laatiaoui, E. Mogilevskiy, S. Raeder, S. Sels, P.V. den Bergh, P.V. Duppen, M. Verlinde, E. Verstraelen, M. Nabuurs, D. Reynaerts, P. Papadakis, Phys. Rev. X **8**(4), 041008 (2018). https://doi.org/10.1103/physrevx.8.041008

125. R. Ferrer, B. Bastin, D. Boilley, P. Creemers, P. Delahaye, E. Liénard, X. Fléchard, S. Franchoo, L. Ghys, M. Huyse, Y. Kudryavtsev, N. Lecesne, H. Lu, F. Lutton, E. Mogilevskiy, D. Pauwels, J. Piot, D. Radulov, L. Rens, H. Savajols, J. Thomas, E. Traykov, C.V. Beveren, P.V. den Bergh, P.V. Duppen, Nucl. Instrum. Methods Phys. Res. Sect. B **317**, 570 (2013). https://doi.org/10.1016/j.nimb.2013.07.028

126. Y. Kudryavtsev, P. Creemers, R. Ferrer, C. Granados, L. Gaffney, M. Huyse, E. Mogilevskiy, S. Raeder, S. Sels, P.V. den Bergh, P.V. Duppen, A. Zadvornaya, Nucl. Instrum. Meth. Phys. Res. B **376**, 345 (2016). https://doi.org/10.1016/j.nimb.2016.02.040

127. M. Ferrer, E. Verlinde, A. Verstraelen, M. Claessens, S. Huyse, Yu. Kraemer, J. Kudryavtsev, P. Van. Romans, P. den Bergh, A. Van Duppen, O. Zadvornaya, G. Chazot, V.I. Grossir, M. Kalikmanov, D. Nabuurs, Reynaerts. Phys. Rev. Res. **3**, 043041 (2021). https://doi.org/10.1103/PhysRevResearch.3.043041

128. S. Raeder, M. Block, P. Chhetri, R. Ferrer, S. Kraemer, T. Kron, M. Laatiaoui, S. Nothhelfer, F. Schneider, P.V. Duppen, M. Verlinde, E. Verstraelen, T. Walther, A. Zadvornaya, Nucl. Instrum. Methods Phys. Res. Sect. B **463**, 272 (2020). https://doi.org/10.1016/j.nimb.2019.05.016

129. R.D. Herzberg, P. Greenlees, P. Butler, G. Jones, M. Venhart, I. Darby, S. Eeckhaudt, K. Eskola, T. Grahn, C. Gray-Jones et al., Nature **442**(7105), 896 (2006). https://doi.org/10.1038/nature05069

130. F. Heßberger, S. Hofmann, D. Ackermann, V. Ninov, M. Leino, G. Münzenberg, S. Saro, A. Lavrentev, A. Popeko, A. Yeremin, C. Stodel, Eur. Phys. J. A **12**(1), 57 (2001). https://doi.org/10.1007/s100500170039

131. F.P. Heßberger, S. Hofmann, D. Ackermann, P. Cagarda, R.D. Herzberg, I. Kojouharov, P. Kuusiniemi, M. Leino, R. Mann, Eur. Phys. J. A **22**(3), 417 (2004). https://doi.org/10.1140/epja/i2003-10238-4

132. F.P. Heßberger, S. Antalic, B. Streicher, S. Hofmann, D. Ackermann, B. Kindler, I. Kojouharov, P. Kuusiniemi, M. Leino, B. Lommel, R. Mann, K. Nishio, S. Saro, B. Sulignano, Eur. Phys. J. A **26**(2), 233 (2005). https://doi.org/10.1140/epja/i2005-10171-6

133. F.P. Heßberger, S. Hofmann, D. Ackermann, S. Antalic, B. Kindler, I. Kojouharov, P. Kuusiniemi, M. Leino, B. Lommel, R. Mann, K. Nishio, A.G. Popeko, B. Sulignano, S. Saro, B. Streicher, M. Venhart, A.V. Yeremin, Eur. Phys. J. A **29**(2), 165 (2006). https://doi.org/10.1140/epja/i2006-10083-y

134. F. Heßberger, S. Hofmann, D. Ackermann, S. Antalic, B. Kindler, I. Kojouharov, P. Kuusiniemi, M. Leino, B. Lommel, R. Mann et al., Eur. Phys. J. A **30**(3), 561 (2006). https://doi.org/10.1140/epja/i2006-10137-2

135. B. Sulignano, S. Heinz, F. Heßberger, S. Hofmann, D. Ackermann, S. Antalic, B. Kindler, I. Kojouharov, P. Kuusiniemi, B. Lommel et al., Eur. Phys. J. A **33**(4), 327 (2007). https://doi.org/10.1140/epja/i2007-10469-3

136. S. Antalic, F.P. Heßberger, S. Hofmann, D. Ackermann, S. Heinz, B. Kindler, I. Kojouharov, P. Kuusiniemi, M. Leino, B. Lommel, R. Mann, Š Šáro, Eur. Phys. J. A **43**, 35 (2010). https://doi.org/10.1140/epja/i2009-10896-0

137. F. Heßberger, S. Antalic, B. Sulignano, D. Ackermann, S. Heinz, S. Hofmann, B. Kindler, J. Khuyagbaatar, I. Kojouharov, P. Kuusiniemi et al., Eur. Phys. J. A **43**(1), 55 (2010). https://doi.org/10.1140/epja/i2009-10899-9

138. S. Antalic, F.P. Heßberger, D. Ackermann, S. Heinz, S. Hofmann, Z. Kalaninová, B. Kindler, J. Khuyagbaatar, I. Kojouharov, P. Kuusiniemi, M. Leino, B. Lommel, R. Mann, K. Nishio, Š Šáro, B. Streicher, B. Sulignano, M. Venhart, Eur. Phys. J. A **47**, 62 (2011). https://doi.org/10.1140/epja/i2011-11062-y

139. F. Hessberger, Eur. Phys. J. A **48**, 75 (2012). https://doi.org/10.1140/epja/i2012-12075-8

140. S. Antalic, F. Heßberger, D. Ackermann, S. Heinz, S. Hofmann, B. Kindler, J. Khuyagbaatar, B. Lommel, R. Mann, Eur. Phys. J. A **51**, 41 (2015). https://doi.org/10.1140/epja/i2015-15041-0

141. Š Šáro, R. Janik, S. Hofmann, H. Folger, F. Heßberger, V. Ninov, H. Schött, A. Kabachenko, A. Popeko, A. Yeremin, Nucl. Instrum. Methods Phys. Res. Sect. A **381**(2–3), 520 (1996). https://doi.org/10.1016/s0168-9002(96)00651-1

142. M. Kaspar, J. Gerl, GSI Scientific Report 1997 GSI-98-1, 195 (1998)

143. J. Hoffmann, N. Kurz, S. Loechner, S. Minami, W. Ott, I. Rusanov, S. Voltz, P. Wieczorek, GSI Scientific Report 2011 (2012)

144. P. Wieczorek, H. Flemming, IEEE Nuclear Science Symposuim & Medical Imaging Conference (IEEE, 2010). https://doi.org/10.1109/nssmic.2010.5873982

145. V.T. Jordanov, G.F. Knoll, Nucl. Instrum. Methods Phys. Res. Sect. A **345**(2), 337 (1994). https://doi.org/10.1016/0168-9002(94)91011-1

146. F. Heßberger, G. Münzenberg, S. Hofmann, W. Reisdorf, J. Schneider, K.H. Schmidt, H. Schött, P. Armbruster, C.C. Sahm, D. Vermeulen, B. Thuma, GSI Sci. Rep. GSI **82–1**, 66 (1982)

147. F. Heßberger, G. Münzenberg, S. Hofmann, W. Reisdorf, K.H. Schmidt, H.J. Schött, P. Armbruster, R. Hingmann, B. Thuma, D. Vermeulen, Z. Phys. A **321**(2), 317 (1985). https://doi.org/10.1007/bf01493453

148. F. Heßberger, G. Münzenberg, S. Hofmann, Y. Agarwal, K. Poppensieker, W. Reisdorf, K.H. Schmidt, J. Schneider, W. Schneider, H. Schött et al., Z. Phys. A **322**(4), 557 (1985). https://doi.org/10.1007/BF01415134

149. F.P. Heßberger et al., Eur. Phys. J. A **52**(11), 328 (2016). https://doi.org/10.1140/epja/i2016-16328-2

150. A. Ghiorso, M. Nurmia, J. Harris, K. Eskola, P. Eskola, Phys. Rev. Lett. **22**(24), 1317 (1969). https://doi.org/10.1103/PhysRevLett.22.1317

151. C.E. Bemis Jr., R.J. Silva, D.C. Hensley, O.L. Keller Jr., J.R. Tarrant, L.D. Hunt, P.F. Dittner, R.L. Hahn, C.D. Goodman, Phys. Rev. Lett. **31**(10), 647 (1973). https://doi.org/10.1103/PhysRevLett.31.647

152. F.P. Heßberger et al., GSI Rep. **85**(10), 11–85 (1985)

153. F. Heßberger, S. Hofmann, V. Ninov, P. Armbruster, H. Folger, G. Münzenberg, H. Schött, A. Popeko, A. Yeremin, A. Andreyev et al., Z. Phys. A **359**(4), 415 (1997). https://doi.org/10.1007/s002180050422

154. F.P. Heßberger, EPJ Web Conf. **131**, 02005 (2016). https://doi.org/10.1051/epjconf/201613102005

155. Z.G. Gan, J.S. Guo, X.L. Wu, Z. Qin, H.M. Fan, X.G. Lei, H.Y. Liu, B. Guo, H.G. Xu, R.F. Chen, C.F. Dong, F.M. Zhang, H.L. Wang, C.Y. Xie, Z.Q. Feng, Y. Zhen, L.T. Song, P. Luo, H.S. Xu, X.H. Zhou, G.M. Jin, Z. Ren, Eur. Phys. J. A **20**(3), 385 (2004). https://doi.org/10.1140/epja/i2004-10020-2

156. F.P. Heßberger et al., Eur. Phys. J. A **52**(7), 192 (2016). https://doi.org/10.1140/epja/i2016-16192-0

157. A. Chatillon, C. Theisen, P. Greenlees, G. Auger, J. Bastin, E. Bouchez, B. Bouriquet, J. Casandjian, R. Cee, E. Clément et al., Eur. Phys. J. A **30**(2), 397 (2006). https://doi.org/10.1140/epja/i2006-10134-5

158. S. Hofmann, F.P. Heßberger, D. Ackermann, S. Antalic, P. Cagarda, S. Ćwiok, B. Kindler, J. Kojouharova, B. Lommel, R. Mann, Eur. Phys. J. A **10**(1), 5 (2001). https://doi.org/10.1007/s100500170137

159. S. Tandel, T. Khoo, D. Seweryniak, G. Mukherjee, I. Ahmad, B. Back, R. Blinstrup, M. Carpenter, J. Chapman, P. Chowdhury et al., Phys. Rev. Lett. **97**(8), 082502 (2006). https://doi.org/10.1103/PhysRevLett.97.082502

160. F. Hessberger, Int. J. Mod. Phys. E **15**(02), 284 (2006). https://doi.org/10.1142/S0218301306004119

161. F. Hessberger, Phys. At. Nucl. **70**(8), 1445 (2007)
162. D. Ackermann, Progress Theor. Phys. Suppl. **196**, 255 (2012). https://doi.org/10.1143/ptps.196.255
163. J. Wild, E. Hulet, R. Lougheed, K. Moody, B. Bandong, R. Dougan, A. Veeck, J. Alloys Compd. **213–214**, 86 (1994). https://doi.org/10.1016/0925-8388(94)90885-0
164. C. E. Bemis, Jr., Robert L. Ferguson, Franz Plasil, R. J. Silva, Frances Pleasonton, and R. L. Hahn, Phys. Rev. C **15**, 705 (1977) https://doi.org/10.1103/PhysRevC.15.705
165. F.P. Heßberger, Spontaneous fission properties of superheavy elements. Eur. Phys. J. A **53**, 75 (2017). https://doi.org/10.1140/epja/i2017-12260-3
166. J. Unik, J. Gindler, L. Glendenin, K. Flynn, A. Gorski, R. Sjoblom, Proc. of the IAEA Symposium 'Physics and Chemistry of Fission', Vol. II, page 19 ff., Rochester, New York, August 13–17, 1973, IAEA, Vienna (1974)
167. V.E. Viola, K. Kwiatkowski, M. Walker, Phys. Rev. C **31**(4), 1550 (1985). https://doi.org/10.1103/physrevc.31.1550
168. J. Khuyagbaatar, A. Yakushev, C. Düllmann, D. Ackermann, L.L. Andersson, M. Block, H. Brand, D. Cox, J. Even, U. Forsberg, P. Golubev, W. Hartmann, R.D. Herzberg, F. Heßberger, J. Hoffmann, A. Hübner, E. Jäger, J. Jeppsson, B. Kindler, J. Kratz, J. Krier, N. Kurz, B. Lommel, M. Maiti, S. Minami, A. Mistry, C. Mrosek, I. Pysmenetska, D. Rudolph, L. Sarmiento, H. Schaffner, M. Schädel, B. Schausten, J. Steiner, T.T.D. Heidenreich, J. Uusitalo, M. Wegrzecki, N. Wiehl, V. Yakusheva, Phys. Rev. Lett. (2015). https://doi.org/10.1103/physrevlett.115.242502
169. T. Huang, W. Zhang, M. Sun, Z. Liu, J. Wang, X. Liu, B. Ding, Z. Gan, L. Ma, H. Yang, Z. Zhang, L. Yu, J. Jiang, K. Wang, Y. Wang, M. Liu, Z. Li, J. Li, X. Wang, H. Lu, A. Feng, C. Lin, L. Sun, N. Ma, D. Wang, F. Zhang, W. Zuo, X. Zhou, H. Xu, G.Q. Xiao, Phys. Rev. C **98**, 044302 (2018). https://doi.org/10.1103/PhysRevC.98.044302
170. A.N. Andreyev, D.D. Bogdanov, V.I. Chepigin, Y.A. Cherepanov, A.P. Kabachenko, O.N. Malyshev, K.V. Mikchajlov, Y.A. Muzychka, G.S. Popeko, B.I. Pustylinik, R.N. Sagaidak, G.M. Ter-Akopian, A.V. Yeremin, AIP Conf. Proc. (1992). https://doi.org/10.1063/1.42004
171. H.M. Devaraja, S. Heinz, O. Beliuskina, V. Comas, S. Hofmann, C. Hornung, G. Münzenberg, K. Nishio, D. Ackermann, Y.K. Gambhir, M. Gupta, R.A. Henderson, F.P. Heßberger, J. Khuyagbaatar, B. Kindler, B. Lommel, K.J. Moody, J. Maurer, R. Mann, A.G. Popeko, D.A. Shaughnessy, M.A. Stoyer, A.V. Yeremin, Phys. Lett. B **748**, 199 (2015). https://doi.org/10.1016/j.physletb.2015.07.006
172. C. Lorenz, L.G. Sarmiento, D. Rudolph, D.E. Ward, M. Block, F.P. Heßberger, D. Ackermann, L.L. Andersson, M.L. Cortés, C. Droese, M. Dworschak, M. Eibach, U. Forsberg, P. Golubev, R. Hoischen, I. Kojouharov, J. Khuyagbaatar, D. Nesterenko, I. Ragnarsson, H. Schaffner, L. Schweikhard, S. Stolze, J. Wenzl, Phys. Rev. C (2017). https://doi.org/10.1103/physrevc.96.034315
173. R. Clark, K. Gregorich, J. Berryman, M. Ali, J. Allmond, C. Beausang, M. Cromaz, M. Deleplanque, I. Dragojević, J. Dvorak, P. Ellison, P. Fallon, M. Garcia, J. Gates, S. Gros, H. Jeppesen, D. Kaji, I. Lee, A. Macchiavelli, K. Morimoto, H. Nitsche, S. Paschalis, M. Petri, L. Stavsetra, F. Stephens, H. Watanabe, M. Wiedeking, Phys. Lett. B **690**(1), 19 (2010). https://doi.org/10.1016/j.physletb.2010.04.079
174. W. Barth, et al., EPJ Web Conf. **138**, 01026 (2017). https://doi.org/10.1051/epjconf/201713801026
175. J. Khuyagbaatar, A. Yakushev, C.E. Düllmann, D. Ackermann, L.L. Andersson, M. Asai, M. Block, R.A. Boll, H. Brand, D.M. Cox, M. Dasgupta, X. Derkx, A.D. Nitto, K. Eberhardt, J. Even, M. Evers, C. Fahlander, U. Forsberg, J.M. Gates, N. Gharibyan, P. Golubev, K.E. Gregorich, J.H. Hamilton, W. Hartmann, R.D. Herzberg, F.P. Heßberger, D.J. Hinde, J. Hoffmann, R. Hollinger, A. Hübner, E. Jäger, B. Kindler, J.V. Kratz, J. Krier, N. Kurz, M. Laatiaoui, S. Lahiri, R. Lang, B. Lommel, M. Maiti, K. Miernik, S. Minami, A.K. Mistry, H. Nitsche, J.P. Omtvedt, G.K. Pang, P. Papadakis, D. Renisch, J.B. Roberto, D. Rudolph, J. Runke, K.P. Rykaczewski, L.G. Sarmiento, M. Schädel, B. Schausten, A. Semchenkov, D.A. Shaughnessy, P. Steinegger, J. Steiner, E.E. Tereshatov, P. Thörle-Pospiech, K. Tinschert, T.T.D. Heidenreich, N. Trautmann, A. Türler, J. Uusitalo, M. Wegrzecki, N. Wiehl, S.M.V. Cleve, V. Yakusheva, Phys. Rev. C (2020). https://doi.org/10.1103/physrevc.102.064602
176. A.N. Andreyev, M. Huyse, P.V. Duppen, Rev. Mod. Phys. **85**(4), 1541 (2013). https://doi.org/10.1103/RevModPhys.85.1541
177. A. Såmark-Roth, D. Cox, D. Rudolph, L. Sarmiento, B. Carlsson, J. Egido, P. Golubev, J. Heery, A. Yakushev, S. Åberg, H. Albers, M. Albertsson, M. Block, H. Brand, T. Calverley, R. Cantemir, R. Clark, C. Düllmann, J. Eberth, C. Fahlander, U. Forsberg, J. Gates, F. Giacoppo, M. Götz, S. Götz, R.D. Herzberg, Y. Hrabar, E. Jäger, D. Judson, J. Khuyagbaatar, B. Kindler, I. Kojouharov, J. Kratz,

J. Krier, N. Kurz, L. Lens, J. Ljungberg, B. Lommel, J. Louko, C.C. Meyer, A. Mistry, C. Mokry, P. Papadakis, E. Parr, J. Pore, I. Ragnarsson, J. Runke, M. Schädel, H. Schaffner, B. Schausten, D. Shaughnessy, P. Thörle-Pospiech, N. Trautmann, J. Uusitalo, Phys. Rev. Lett. **126**(3), 032503 (2021). https://doi.org/10.1103/PhysRevLett.126.032503